



Warm cascade states in a forced-dissipated Boltzmann gas of hard spheres

Davide Proment^{a,b,*}, Miguel Onorato^{a,b}, Pietro Asinari^c, Sergey Nazarenko^d

^a Dipartimento di Fisica Generale, Università degli Studi di Torino, Via Pietro Giuria 1, 10125 Torino, Italy

^b INFN, Sezione di Torino, Via Pietro Giuria 1, 10125 Torino, Italy

^c Dipartimento di Energetica, Politecnico di Torino, Corso Duca degli Abruzzi 24, 10129 Torino, Italy

^d Mathematics Institute, The University of Warwick, Coventry, CV4-7AL, UK

ARTICLE INFO

Article history:

Received 15 July 2011

Received in revised form

24 November 2011

Accepted 28 November 2011

Available online 6 December 2011

Communicated by M. Vergassola

Keywords:

Turbulent cascade

Kinetic equations

Kolmogorov–Zakharov solutions

Kinetic theory of gases

Boltzmann equation

ABSTRACT

We study the homogeneous isotropic Boltzmann equation for an open system. For the case of a hard spheres gas, we look for nonequilibrium steady solutions in the presence of forcing and dissipation. Using the language of weak turbulence theory, we analyze the possibility of observing the Kolmogorov–Zakharov steady distributions, i.e. solutions characterized by constant fluxes of conserved quantities. We derive a differential approximation model and we find that the expected nonequilibrium steady solutions have always the form of warm cascades. We propose an analytical prediction for the relation between the forcing and dissipation and the thermodynamic quantities of the system. Specifically, we find that the temperature of the system is independent of the forcing amplitude and determined only by the forcing and dissipation scales. Finally, we perform direct numerical simulations of the Boltzmann equation finding consistent results with our theoretical predictions.

© 2011 Elsevier B.V. All rights reserved.

1. Introduction

Systems in a steady state are characterized by observables that do not change in time; they can be either in equilibrium or out of equilibrium. Systems in nonequilibrium steady states have net currents (fluxes): examples of nonequilibrium steady-state systems include an object in contact with two thermal sources at different temperatures, for which the current is a heat flux; a resistor with electric current flowing across it; the kinesin-microtubule system, for which the kinesin motion is the current. Most biological systems, including molecular machines and even whole cells, are in nonequilibrium states [1]. In particular, biological systems rely on a continuous flux of energy and/or particles supplied by some proper environmental reservoirs.

In statistical mechanics, investigating the general properties of a system in contact with reservoirs, namely an open system, is a long lasting problem (e.g. see the second problem discussed by Lieb on the occasion of the award of the Boltzmann medal [2]), even though these theoretical challenges are sometimes neglected in applied engineering at large. The difficulties arise from the

fact that finding the large deviation functional for a stationary state with fluxes is still an open problem (see [3] and references therein). In the present work, for focusing our attention and considering an affordable goal, we consider the kinetic theory of gases. In particular, we consider a system composed of a large number of interacting particles, comparable to the Avogadro number. The Boltzmann kinetic equation (BKE) describes the time evolution of the single-particle distribution function, which provides a statistical description of the positions and velocities (momenta) of the gas molecules. This integro-differential kinetic equation, proposed by Boltzmann at the end of the XIX century, has been derived starting from the phase-space Liouville equation, assuming the *Stosszahlansatz* [4]. Its equilibrium state, which maximizes the entropy measure, is the Maxwell–Boltzmann distribution. In case of small deviations from the local equilibrium, it is possible to systematically derive the hydrodynamic equations for macroscopic quantities of the system; e.g., in the lowest order approximation for small departures from equilibrium, the Navier–Stokes equations [4].

Kinetic equations have also been studied in the framework of wave turbulence theory [5] where it has been shown that, in the presence of forcing and dissipation, other solutions than the thermodynamic one can be stationary states of the system. These distributions, which usually have the form of power-laws in momentum space, are called the Kolmogorov–Zakharov (KZ) and they represent constant flux of conserved quantities

* Corresponding author at: Dipartimento di Fisica Generale, Università degli Studi di Torino, Via Pietro Giuria 1, 10125 Torino, Italy. Tel.: +39 011 6707454.

E-mail address: davideproment@gmail.com (D. Proment).

URL: <http://www.to.infn.it/~proment> (D. Proment).

similar to the Kolmogorov energy cascade in strong Navier–Stokes turbulence [6,7]. They have been studied for a great variety of weakly nonlinear dispersive models: examples can be found in water waves [8–10], internal waves [11], nonlinear optics [12], the Bose–Einstein condensation [13–15], magnetohydrodynamics [16] and so on.

An out of equilibrium description of the Boltzmann equation using the KZ solutions was first devised in [17] considering different types of interaction potential between particles. Some problems related to the locality of the interactions and wrong flux directions were pointed out. In particular in [18] Kats showed that for all realistic physical situations the direction of the cascades in the system is always in the wrong orientation with respect to the one predicted by the Fjørtoft argument.¹ When a formal KZ solution has a flux direction contradicting with the Fjørtoft argument, this spectrum (even if local) cannot be established because it cannot be matched to any physical forcing and dissipation at both ends of the inertial range. For example in the two-dimensional nonlinear Schrödinger equation model the particle cascade KZ solution was found to be of this type [12]; the authors argued that in this case the KZ solution is not achievable and a mixed state, with both a cascade and a thermodynamic components, was proposed. Another example of mixed cascade-thermodynamic states, named *warm cascades*,² has been found in the context of three-dimensional Navier–Stokes turbulence [19].

The present manuscript will focus on warm cascades found in the homogeneous isotropic Boltzmann equation (HIBE) and in particular it will answer to the following important questions.

- What is precisely the relation between the conserved quantity fluxes and the thermodynamics quantities of the system?
- How does this relation depends on the forcing and dissipation rates and acting scales?

To answer the above questions we will perform numerical simulations of the homogeneous isotropic Boltzmann equation with forcing and dissipation. We will then use a diffusion approximation model (DAM) to derive analytical predictions on how the thermodynamic quantities, temperature and chemical potential, are related to fluxes, forcing and dissipative scales. We will then test these predictions by numerically simulating both DAM and the complete homogeneous isotropic Boltzmann equation.

The work is organized as follows: in Section 2 we review the properties of the Boltzmann equation for the homogeneous isotropic case; in Section 3 we introduce DAM and we derive the analytical predictions; Section 4 is dedicated to numerical results of the DAM and the HIBE; in Section 5 we draw the conclusions. A set of [Appendices](#) also provide detailed calculations of those results which are briefly reported in the main text.

2. The Boltzmann kinetic equation

The Boltzmann kinetic equation describes the time evolution of the single-particle distribution function, which provides a statistical description for the positions and momenta of the gas molecules: the function $n(\mathbf{x}, \mathbf{k}, t)$ express a probability density function in the one-particle phase space $\mathbb{R}_x^d \times \mathbb{R}_k^d$ with respect

to time, where d is the dimension. Note that we denote the momentum variable with the letter \mathbf{k} instead of the conventional \mathbf{p} to follow the common notation of wave turbulence [5]. The Boltzmann equation takes the following form:

$$\frac{\partial n}{\partial t}(\mathbf{x}, \mathbf{k}_1, t) + \frac{\mathbf{k}_1}{m} \cdot \frac{\partial n}{\partial \mathbf{x}}(\mathbf{x}, \mathbf{k}_1, t) = I_{\text{coll}}(\mathbf{x}, \mathbf{k}_1, t), \quad (1)$$

where

$$I_{\text{coll}} = \int_{-\infty}^{+\infty} W_{12}^{34} [n(\mathbf{x}, \mathbf{k}_3, t)n(\mathbf{x}, \mathbf{k}_4, t) - n(\mathbf{x}, \mathbf{k}_1, t)n(\mathbf{x}, \mathbf{k}_2, t)] d\mathbf{k}_2 d\mathbf{k}_3 d\mathbf{k}_4 \quad (2)$$

sums the effect of the two-body collisions of particles with all possible values of momenta. The form of the collision integral we are reporting is equivalent to the standard one and corresponds to Eq. (4.18), page 64 in Cercignani's book [4]. Here W describes synthetically the scattering amplitude transition $2 \rightarrow 2$ as a function of the momenta of the interacting particles. As we consider elastic collisions, the general way to express W is

$$W_{12}^{34} = \Gamma_{12}^{34} \delta(\mathbf{k}_1 + \mathbf{k}_2 - \mathbf{k}_3 - \mathbf{k}_4) \delta(|\mathbf{k}_1|^2 + |\mathbf{k}_2|^2 - |\mathbf{k}_3|^2 - |\mathbf{k}_4|^2), \quad (3)$$

where δ -functions assure conservation of the total momentum and the total kinetic energy (which is proportional to $|\mathbf{k}|^2$) of incoming and outgoing particles. The collision probability, expressed by $\Gamma_{12}^{34} \equiv \Gamma(\mathbf{k}_1, \mathbf{k}_2 | \mathbf{k}_3, \mathbf{k}_4) \geq 0$, is invariant under permutations $\{1, 2\} \rightarrow \{2, 1\}$, $\{3, 4\} \rightarrow \{4, 3\}$, and $\{1, 2\} \rightarrow \{3, 4\}$.

In the present paper we will consider the case of three-dimensional rigid spheres with diameters σ and mass m , for which Γ simply results in $\Gamma_{12}^{34} = 2\sigma^2/m$ [4]. Physically, this choice may have relevance for low temperature rarefied gases near the Bose–Einstein condensation [20,21], (elastic) granular gases [22], or a generic system where, in first approximation, the interaction is very weak at large distance and very strong at small ones ($V(r) = r^{-\alpha}$ with $\alpha \gg 0$). For other interaction potentials, as Coulomb or Van der Waals forces, refer to [23,18].

Note that in the literature the collision integral can take different (but equivalent) operative expressions, depending on the considered dummy variables. Here we have chosen the pre-collision and post-collision particle momenta to take advantage of the formal analogy with the equations used in the weak turbulence theory. The equivalence with the choice of the field particle velocity and the impact unit vector, which is more common in the mathematical community, is explained in [Appendix A](#). Readers should not confuse between our notation where $\Gamma = \text{const.}$ is valid for the three-dimensional hard sphere model and the other notation where the collision cross section is independent of the velocities for the case of the Maxwell molecules. Most of the results discussed below do not apply for the latter model.

For the purposes of our work, we consider a homogeneous and isotropic (in physical space \mathbb{R}_x^d) system with the one-particle probability density function independent of \mathbf{x} and its momentum dependency arising only via the modulus $k = |\mathbf{k}|$, so $n(\mathbf{x}, \mathbf{k}, t) \rightarrow n(k, t)$. It is useful to express the distributions in the energy space $\omega_i = |\mathbf{k}_i|^2$ where we use again the notation ω for the energy in analogy with wave turbulence. Then, the particle density in ω -space satisfies the relation $\int N(\omega, t) d\omega = \int n(k, t) d\mathbf{k}$ or, in the other words, $N(\omega, t) = n(\omega, t) \Omega$, $\omega^{\frac{d-1}{2}} \left| \frac{d\mathbf{k}}{d\omega} \right|$, where Ω is the solid angle. After these considerations, Boltzmann equation (1) simplifies to the homogeneous isotropic Boltzmann equation (HIBE):

$$\frac{\partial N_1}{\partial t} = \int_0^\infty S_{12}^{34} (n_3 n_4 - n_1 n_2) \times \delta(\omega_1 + \omega_2 - \omega_3 - \omega_4) d\omega_2 d\omega_3 d\omega_4, \quad (4)$$

¹ This argument, originally put forward by Fjørtoft in 1953 for the 2D turbulence, says that the integral whose density grows fastest with the wavenumber/momentum must cascade from low to high wavenumbers/momenta. The other integral must cascade inversely, from high to low wavenumbers/momenta. For the classical particles, this means that the energy flux must be from low to high momenta, and the flux of particles must be toward low momenta; see Section 2.3.

² In Navier–Stokes the warm cascades correspond to so called bottleneck phenomenon which arises in numerics due to an energy flux stagnation near the maximum wave-number.

where we denote for brevity $N_i = N(\omega_i, t)$ and $n_i = n(\omega_i, t)$, and the functional

$$S_{12}^{34} = (\omega_1 \omega_2 \omega_3 \omega_4)^{\frac{d-1}{2}} \left| \frac{dk_1}{d\omega_1} \right| \left| \frac{dk_2}{d\omega_2} \right| \left| \frac{dk_3}{d\omega_3} \right| \left| \frac{dk_4}{d\omega_4} \right| \times \int_{\Omega} \Gamma_{12}^{34} \delta(\mathbf{k}_1 + \mathbf{k}_2 - \mathbf{k}_3 - \mathbf{k}_4) d\Omega_1 d\Omega_2 d\Omega_3 d\Omega_4 \quad (5)$$

takes into account the change of coordinates and the average over solid angles. Hereafter, we always consider a three-dimensional gas of hard-sphere particles in a non-dimensional form with $m = 1$ and $\sigma^2 = 8$. Then the functional simply results in $S_{12}^{34} = 2\pi \min[\sqrt{\omega_1}, \sqrt{\omega_2}, \sqrt{\omega_3}, \sqrt{\omega_4}]$ (see Appendix B for details of the angular integration).

The HIBE has two conserved quantities, the mass and energy densities:

$$\rho_M = \int_{-\infty}^{+\infty} n(\omega, t) d\mathbf{k} = 2\pi \int_0^{+\infty} n(\omega, t) \sqrt{\omega} d\omega, \quad (6)$$

$$\rho_E = \int_{-\infty}^{+\infty} n(\omega, t) k^2 d\mathbf{k} = 2\pi \int_0^{+\infty} n(\omega, t) \omega^{\frac{3}{2}} d\omega.$$

Note that ρ_M and ρ_E are always constant in time for any distribution n and interaction potential, due to the fact that collisions are $2 \rightarrow 2$ and elastic. This is evident by evaluating their time derivatives using Eq. (4): the symmetries with respect to the integration indices immediately show that these quantities are zero.

2.1. Steady solutions

2.1.1. Equilibrium in a closed system

The HIBE (4) is an integro-differential equation with no general analytic solution. It is easy, however, to look for steady (time independent) solutions. In closed system, i.e. without forcing and/or dissipation mechanisms, the only steady solution corresponds to the thermodynamic equilibrium described by the Maxwell–Boltzmann (MB) distribution:

$$n_{\text{MB}}(\omega) = e^{-\frac{\omega + \mu}{T}} = A e^{-\frac{\omega}{T}}, \quad (7)$$

where $A = e^{-\frac{\mu}{T}}$ and constants μ and T have the meaning of the chemical potential and the temperature, respectively (we consider the natural unit system, where the Boltzmann constant is one). To verify the solution, it is sufficient to plug (7) into (4): for any value of T , μ and the interaction potential S_{12}^{34} , the δ -function assures that the integrand is zero. Moreover, the total mass density of the system is $\rho_M = A(\pi T)^{\frac{3}{2}}$, the total energy density is $\rho_E = \frac{3}{2} A \pi^{\frac{3}{2}} T^{\frac{5}{2}}$, and any other moment of ω , due to the bi-parametric nature of the MB distribution, is a function of ρ_M and ρ_E . The H theorem states that in a closed system any out of equilibrium distribution with defined mass and energy densities will always relax to the MB distribution having the same ρ_M and ρ_E .

In Fig. 1 we show a numerical simulation of the HIBE with initial condition given by a Gaussian function centered around a particular value of energy; as it is clear from the figure, the initial condition relaxes to the MB distribution. The numerical algorithm used to perform this simple example is presented in the first two paragraphs of Section 4.2. We can observe that the initial condition evolves reaching an equilibrium MB distribution: the exponential behavior become evident by observing the inset where the plot is reported in lin-log scale. Moreover, by fitting the results with the MB function we can find the thermodynamic quantities A and T : those correspond exactly to ones expected from the knowledge of the initial mass and the energy densities (note that now integrals (6) are evaluated from 0 to a finite value of ω due to numerical finiteness of ω -space).

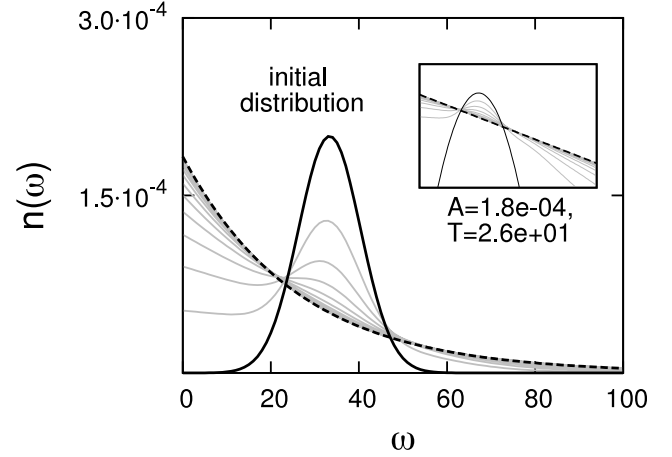


Fig. 1. Numerical computation of the HIBE in an initial Gaussian shaped distribution (continuous black line); intermediate states are shown with gray lines and final steady distribution in a dashed black line. The latter has the MB behavior (7) with fitted parameters A and T reported in the figure. The inset shows the same plot in the lin-log scale.

2.1.2. Non-equilibrium steady states

Now, what can we expect in an open system driven by external forcing and dissipation mechanisms? We will answer this question keeping in mind the main results of the wave turbulence theory. Part of this theory is dedicated to study steady solutions of kinetic equations in the power-law form, $n(\omega) \sim \omega^{-x}$, where the constant x assumes different values depending on the considered wave system. Indeed, it is sometimes possible to find the so-called Kolmogorov–Zakharov (KZ) solutions $n_{\text{KZ}}(\omega) \sim \omega^{-x}$ which correspond to constant fluxes of conserved quantities through scales. The KZ distribution always appears in a range of scales, known as the inertial range, between the forcing and dissipation where the source and sink are located.

As already mentioned, the HIBE conserves the number of particles and the energy, therefore one could expect to observe two turbulent KZ cascades. The KZ exponent x can be evaluated by applying the standard Zakharov transformations [5], by dimensional analysis [24], or by using the method (equivalent to Zakharov transformation) proposed by Balk [25]. We have chosen the last one and the complete analytical calculations are presented in Appendix C. The KZ exponents depend on the scaling behavior of the scattering term Γ_{12}^{34} and on the dimension d of the particle system. For the particular case of three-dimensional hard spheres we have

$$\begin{aligned} \text{constant particle flux } \eta &\implies n_{\text{KZ}}(\omega) \sim \omega^{-\frac{7}{4}}, \\ \text{constant energy flux } \epsilon &\implies n_{\text{KZ}}(\omega) \sim \omega^{-\frac{9}{4}}. \end{aligned} \quad (8)$$

The simplest way to mimic an open system where steady nonequilibrium distributions of the form of turbulent KZ solutions can be establish is to consider a forced-dissipated HIBE:

$$\frac{\partial N(\omega_1, t)}{\partial t} = I_{\text{coll}}(\omega_1, t) + F(\omega_1) - D(\omega_1)N(\omega_1). \quad (9)$$

The forcing F is constant in time and very narrow near a particular energy value ω_f : with this choice the incoming fluxes of particles η and energy ϵ roughly satisfy relation $\epsilon = \omega_f \eta$. The dissipation term D is implemented as a filter which removes, at each iteration time, energy and particles outside of the domain $\omega \in (\omega_{\min}, \omega_{\max})$. Further details on the numerical scheme are explained in first two paragraphs of Section 4.2.

From the theoretical point of view, the introduction of forcing and dissipation is desirable so that the resulting non-equilibrium

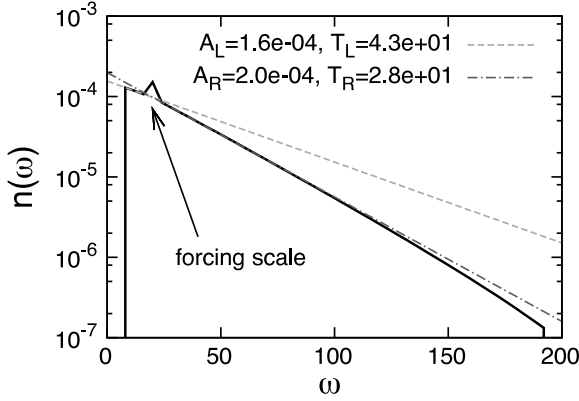


Fig. 2. An example of the HIBE (9) steady state shown in a black line in the lin-log scale. Simulation parameters are: $\omega_{\min} = 5$, $\omega_f = 22$, $\omega_{\max} = 195$ and $F = 10^{-5}$, and $\omega_{\text{cutoff}} = 200$. The dashed and point/dashed lines are the left and right branch best fits obtained with the MB distribution (7): fitting parameters are reported in label.

distribution can reach its steady state—a system which is easier to understand and to study than evolving non-equilibrium systems. Separating the forcing and the dissipation scales corresponds to the classical setup in turbulence in which a pure cascade-dominated non-equilibrium steady state forms in the inertial range of scales between the forcing and the dissipation. This is a formal setup for the Richardson energy cascade and the respective Kolmogorov spectrum in 3D hydrodynamic turbulence, and for the Kraichnan dual cascade in 2D turbulence.

Physically, examples of forcing may be externally produced by beams, e.g. neutral beam injection in tokamak plasmas, or fast particles entering into the atmosphere from space, or particles with a particular range of energy/momenta produced by a chemical or a nuclear reaction. The dissipation could be represented by a loss of particles via a chemical or a nuclear reaction when they reach a certain reaction threshold energy, or simply via a loss of particles leaving the system, e.g. when reaching energies higher than the potential barrier of a retaining trap. Therefore, real physical experiments to test the model (9) may be for example: thermal cloud in the Bose–Einstein condensate gases [26], out-of-equilibrium chemical solutions, and nuclear reactions where particles are produced around a particular energy value. Of course, if the experimental setup is formed by particles behaving with an interaction potential different from the hard sphere case, new scaling coefficients (8) must be evaluated and the following predictions modified. Finally, regarding granular gases, we underline that in this latter system the dissipative term, consequence of the inelastic collisions, acts at all velocity scales, contradicting our hypothesis of wide scale separation between forcing and damping. For that reason, even if a granular gas is an out-of-equilibrium system where steady solutions are reached thanks only to a forcing term [27–29], it is very far from our idealized system.

What behavior should one expect for the forced/damped integro-differential system described by Eq. (9)? In Figs. 2 and 3 we plot the nonequilibrium steady states obtained with numerical simulations of the HIBE with forcing and dissipation; the initial conditions are characterized by $n(\omega, t = 0) = 0$. The parameters in the simulations are $\omega_{\min} = 5$, $\omega_{\max} = 195$, the forcing rate $F = 10^{-5}$. In Fig. 2 forcing is located at $\omega_f = 22$ and in Fig. 3 at $\omega_f = 182$. No KZ solutions (8) are observed (note that both plots are in lin-log scales) and weakly perturbed exponential curves can be observed. We can attempt to measure the quantities T and A in (7) by fitting our numerical curves; however, those are not perfect straight lines (in the lin-log plot) and left and right branches with respect to forcing scale may give different results. For such reason

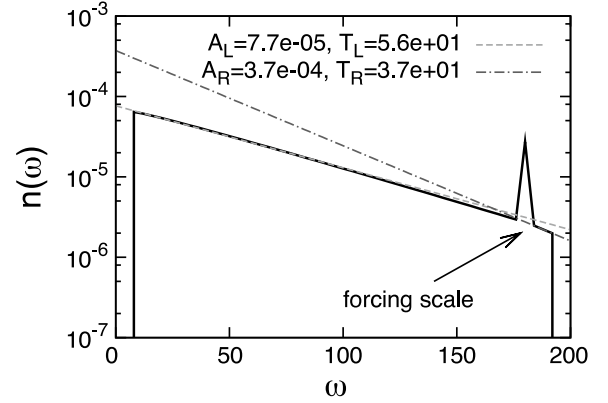


Fig. 3. An example of the HIBE (9) steady state shown in a black line in the lin-log scale. Simulation parameters are: $\omega_{\min} = 5$, $\omega_f = 182$, $\omega_{\max} = 195$ and $F = 10^{-5}$, and $\omega_{\text{cutoff}} = 200$. The dashed and point/dashed lines are left and right branch best fits obtained with the MB distribution (7): fitting parameters are reported in label.

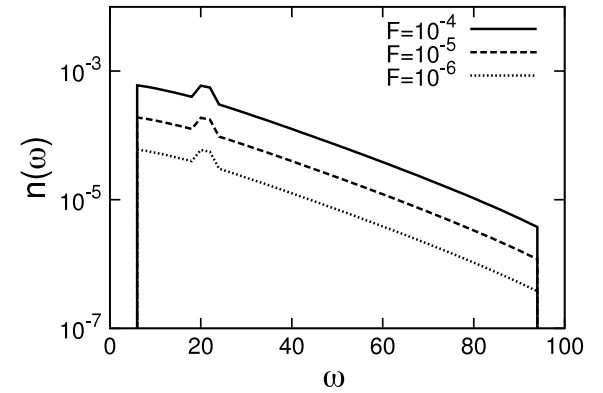


Fig. 4. Steady states of the HIBE (9) in the lin-log scale obtained for different values of the forcing rate F . Parameters are $\omega_{\text{cutoff}} = 200$, $\omega_{\min} = 5$, $\omega_f = 21$ and $\omega_{\max} = 95$.

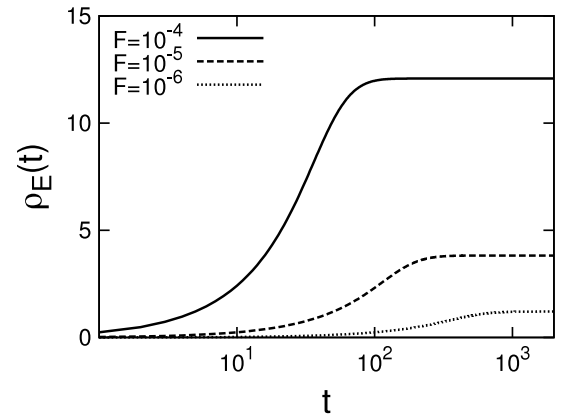


Fig. 5. Total energy densities $\rho_E(t)$ in function of time for different forcing rates F . For the system parameters refer to ones in Fig. 4.

we will denote by $(\cdot)_L$ the quantities evaluate on the left branch and with $(\cdot)_R$ the right ones.

Another example we have analyzed is the case where we fix the forcing and dissipative scales and change the forcing rate. Numerical results for final steady states evaluated for three different forcing amplitudes, $F = 10^{-4}, 10^{-5}, 10^{-6}$, are presented in Fig. 4. The effect of increasing the amplitude F results in an upward shift of the curves. Therefore, qualitatively, the temperature appears to be the same for each value of the flux. The only difference is the speed at which the system, initially empty, reaches its steady state. In Fig. 5 we show the energy density evolution.

After these preliminary numerical results, a lot of questions can be posed. Why no KZ constant flux solutions are observed but just small deviations from MB distributions? What happens when forcing or dissipation scales are changed? What is in general the relation between physical quantities such as fluxes, forcing and dissipation scales and the MB parameters? The aim of this paper is to provide explanations to such phenomena and answer the above questions.

2.2. Locality of interactions

For the KZ spectra to be valid mathematical (and therefore physically relevant) solutions, it is necessary that they satisfy the locality condition. A spectrum is local when the collision integral converges. In other words, non-locality means that the collision integral is not weighted scale by scale but most of the contributions come from the limits of integration corresponding to the ends of the inertial range. Physically, the non-locality is in contradiction with the assumption that the flux of the relevant conserved quantity in the inertial range is carried only by the nearest scales. Mathematically, locality guaranties that the KZ spectrum is a valid solution in an infinite inertial range, which is not guaranteed *a priori* because Zakharov transformation is not an identity transformation and could, therefore, lead to spurious solutions.

For the HIBE case, locality depends on the particular interaction potential, which affects the scaling of Γ_{12}^{34} , and on the dimensionality of the system—for detailed calculations see Appendix C. Locality is not always found for both KZ solutions: for example for the Coulomb potential only the energy cascade is local, as shown in [17]. In the case of three-dimensional hard spheres considered in the present work, the criterion of locality is never satisfied for any of the two KZ solutions, which means that these solutions are un-physical and irrelevant in this model.

2.3. The flux directions

Besides locality, another important requirement for establishment of the KZ spectra is the correctness of the flux directions for the respective conserved quantities. In a system where two quantities are conserved, the following Fjørtoft-type argument is used to establish which quantity must have a direct or an inverse cascade.

2.3.1. The Fjørtoft argument

Consider an open system where forcing scale ω_f is widely separated from a low- ω dissipation scale ω_{\min} and a high- ω dissipation scale ω_{\max} , thus $\omega_{\min} \ll \omega_f \ll \omega_{\max}$. Because the energy density in the ω -space is different from the particle density by factor ω , the forcing rate of the energy ϵ is related with the forcing rate of the particles η as $\epsilon \sim \omega_f \eta$. Suppose that some energy is dissipated at the low scale ω_{\min} at a rate comparable with the forcing rate ϵ . But then the particles would have to be dissipated at this scale at the rate proportional to $\epsilon/\omega_{\min} \sim \eta \omega_f/\omega_{\min} \gg \eta$, which is impossible in steady state because the dissipation cannot exceed the forcing. Thus we conclude that in the steady state the energy must dissipate only at ω_{\max} . By a symmetric argument one can easily show that the only place where the particles can be dissipated in such systems is ω_{\min} . This means that energy must have a direct cascade (positive flux direction) and particles an inverse cascade (negative flux direction).

2.3.2. Flux directions in the HIBE

It has been proved in [18], see also Appendix C for details, that fluxes of the KZ solutions for a wide range of interaction coefficient Γ (for example Coulomb interaction potential, Maxwell

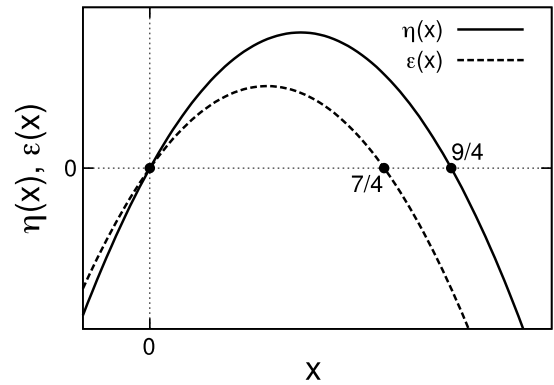


Fig. 6. Energy and particle fluxes on power-law solutions $n(\omega, t) \sim \omega^{-x}$ as functions of x for the three-dimensional hard sphere model.

molecules or hard spheres³) have an opposite direction with respect to the Fjørtoft argument requirements. An alternative way for finding the sign of the fluxes is considering them for general (not necessarily steady) power-law spectra $n(\omega, t) \sim \omega^{-x}$ and plotting them as functions of x for a fixed (ω, t) , see Fig. 6. Three exponents x correspond to steady solutions of the HIBE: the particle equipartition $x_{\text{eq}} = 0$, the KZ particle cascade x_η and the KZ energy cascade x_ϵ . As shown in Appendix C, we know that $\epsilon = 0$ on the particle cascade, $\eta = 0$ on the energy cascade, whereas in the equipartition both fluxes are zero, i.e. $\epsilon = \eta = 0$. We also know that for large negative x (large positive slope) both fluxes must be negative, as such a steep unsteady spectrum would evolve to become less steep, toward equipartition. Note that always $x_\eta < x_\epsilon$, when $x > 0$. Now we can sketch the particle and energy fluxes as a function of the exponent x as it is done in Fig. 6. From this sketch, it can be easily understood that whenever the condition $x_\eta < x_\epsilon$ is valid, the particle flux will be positive and the energy flux will be negative, contradicting the Fjørtoft argument. This means that one cannot match these formal KZ solutions, obtained for an infinite inertial range, to any physical forcing or dissipation at the ends of a large (but finite) inertial range.

What is then happening when fluxes have an opposite direction with respect to the one expected from the Fjørtoft argument? It has been observed in optical wave turbulence [12] that the pure KZ spectra are not established in these cases and one has to expect a mixed solution where both a flux and a thermal components are present. Such mixed states are quite common for turbulent systems of different kinds, including strong Navier–Stokes turbulence and have been named *warm cascades* [19]. Such cascades were obtained within the Leith model (which belongs to the class of the differential approximation models) as exact analytical solutions.

3. Differential approximation model

Numerical integration of the Boltzmann collision integral is very challenging. A great simplification comes from the isotropic assumption, which reduces the collision integral to a two-dimensional one. However spanning a large number of momentum scales is still difficult. For those reasons, some approximations to the kinetic equations were proposed in order to increase the range of modeled scales, see for example [30].

A great simplification is to replace the collision integral operator of the kinetic equation by a nonlinear differential operator which mimics the basic scalings of the original one and yields the same

³ Kats found that for an interaction potential $V(r) \sim r^{-\alpha}$ the fluxes are in the wrong direction with respect to the Fjørtoft argument when $\alpha < 0$ or $\alpha > 4/7$.

steady solutions. The HIBE then results in a nonlinear partial differential equation called the differential approximation model (DAM). Such models have been proposed to simulate turbulence in different research fields: for example in water waves [31], in nonlinear optics [12], in strong Navier–Stokes turbulence [32–34], in Kelvin quantum turbulence [35], in astrophysics (Kompaneets equation) [36], in semiconductors [37]. Replacing the integral operator by a differential one amounts to assuming locality of the scale interactions, which means the relevant distributions must be local for the DAM to have a good predictive power. We mentioned in Section 2 that for hard sphere Boltzmann equation the pure KZ spectra are non-local and so no DAM would be advisable. However, we observed in some examples (Figs. 2 and 3) that the relevant solutions in this case are not pure KZ spectra but distributions which are close to MB, warm cascades, which appear to be local. Thus, we use the DAM for describing this system, after which we will validate our results by computing the full HIBE.

For the dual cascade systems, such as gravity water waves [38], nonlinear optics [12], two-dimensional hydrodynamic turbulence [33], Kelvin waves [35] or the HIBE considered here, the DAM has always the form of a dual conservation law,

$$\partial_t N(\omega, t) = \partial_{\omega\omega} R[n(\omega, t)], \quad (10)$$

where R is a nonlinear second-order differential term whose details depend on the particular model. This equation can be written as a continuity equation for the particle invariant,

$$\partial_t N(\omega, t) + \partial_\omega \eta(\omega, t) = 0,$$

with the particle flux

$$\eta(\omega, t) = -\partial_\omega R[n(\omega, t)]. \quad (11)$$

Moreover, Eq. (10) can be written as a continuity equation for the energy [12],

$$\partial_t [N(\omega, t)\omega] + \partial_\omega \epsilon(\omega, t) = 0,$$

with the energy flux

$$\epsilon(\omega, t) = R[n(\omega, t)] - \omega \partial_\omega R[n(\omega, t)]. \quad (12)$$

We are now able to find the functional R by requiring it to yield the MB distribution (7) and the KZ spectra (8) as steady state solutions of the DAM (10). These constraints lead to

$$R[n(\omega, t)] = -S\omega^{\frac{13}{2}} n^2(\omega, t) \partial_{\omega\omega} \log n(\omega, t), \quad (13)$$

where S is a constant. A formal derivation starting from the kinetic equation can be obtained following [12,37] and is presented in Appendix D. It is trivial to verify by substitution that KZ solutions (8) correspond to constant fluxes through scales. Namely, the KZ particle cascade has a constant particle flux and zero energy flux while the KZ energy cascade vice versa. Let us again consider the flux directions on the KZ distributions, but now using the DAM. Substituting the power-law $n = c\omega^{-x}$ into (13), Eqs. (11) and (12) yield

$$\begin{aligned} \eta &= c^2 S x (9/2 - 2x) \omega^{7/2-2x} \\ \epsilon &= c^2 S x (11/2 - 2x) \omega^{9/2-2x}. \end{aligned} \quad (14)$$

By plotting η and ϵ as functions of the exponent x at fixed ω , we arrive again at Fig. 6. Note that, by using the DAM, such a plot was obtained. Once again we note that the particle and the energy fluxes on the respective KZ solutions ($x = 7/4$ and $x = 9/4$) have opposite directions with respect to the Fjørtoft argument prediction.

The beauty of the DAM is the possibility to solve numerically the system for wide frequency ranges and, therefore, to find clear scalings. In particular, such models are very efficient for finding constant steady flux solutions because they become simple ordinary differential equations (ODEs). In the following we will present some analytical results for such steady states.

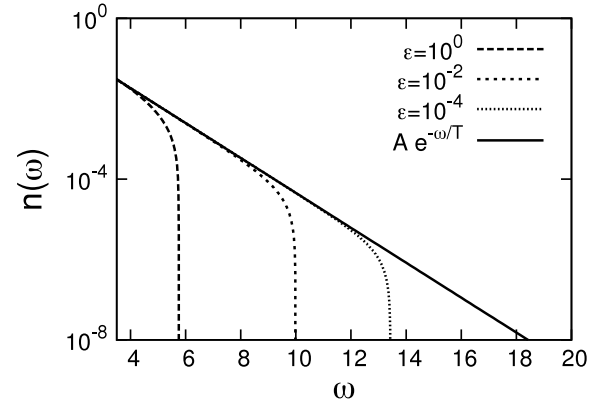


Fig. 7. DAM simulations of (16) for different constant energy flux ϵ starting with the same initial condition at $\omega_0 = 3.5$ given by the MB distribution $n_{MB}(\omega) = Ae^{-\omega/T}$ where $A = 1$ and $T = 1$ (continuous line).

3.1. Constant energy flux: direct cascade

We will now find an ODE that describes a constant direct energy cascade ϵ with no flux of particles, which we call ODE- ϵ . According to Fjørtoft argument, this implies a large direct-cascade inertial range. Setting $\eta = 0$ in (11) and (12), we have

$$\text{constant energy flux} \implies \epsilon = R(\omega, t) = \text{const.} \quad (15)$$

Using (13), we arrive at the following Cauchy problem

$$\begin{cases} \epsilon = -S\omega^{\frac{13}{2}} n^2(\omega) \partial_{\omega\omega} \log n(\omega), \\ n(\omega_0) = n_0, \\ \partial_\omega n(\omega_0) = n'_0, \end{cases} \quad (16)$$

where we have chosen the boundary conditions fixing the values of the distribution and its derivative at the same point ω_0 (e.g. at the forcing scale) for ease of numerical solution.

If we solve numerically in ω -forward the ODE- ϵ for different values of the energy flux we find the curves presented in Fig. 7. Here we do not want to discuss the details (it will be done widely in Section 4), but just remark that the solutions follow the MB distribution and suddenly change behavior going very fast to a zero value of the distribution. We will call this rapid change a *front solution*.

3.1.1. Compact front behavior

It is possible to find a front solution for the Eq. (15) describing the behavior near the dissipation scale. Let us seek for a front solution which in the vicinity of a certain point ω_{\max} behaves like $n(\omega) = B(\omega_{\max} - \omega)^\sigma$. If we plug this expression into (15) and take the limit $\omega \rightarrow \omega_{\max}$ we find that to satisfy this equation in the leading order in $(\omega_{\max} - \omega)$ we must have

$$\begin{cases} \sigma = 1 \\ B = \sqrt{\frac{\epsilon}{S\omega_{\max}^{13/2}}} \implies n(\omega) = \sqrt{\frac{\epsilon}{S\omega_{\max}^{13/2}}} (\omega_{\max} - \omega). \end{cases} \quad (17)$$

Thus, the front solution is linear in the vicinity of ω_{\max} with a slope depending on the dissipation scale ω_{\max} and the value of the energy flux ϵ . Note that the compact front behavior at the dissipation scale is typical for the DAM. We will soon discover that ω_{\max} is a very useful physical parameter which allows us to find a link between the temperature, the chemical potential and the energy flux in the forced-dissipated system.

3.1.2. The Kats–Kontorovich correction

Let us summarize our preliminary observations. We expect a warm cascade, that is a distribution which contains both the flux

and the thermal components. We have also found that the solution has a compact front which arrests the cascade at the dissipation scale ω_{\max} . We will now assume (verifying it later) that in the most of the inertial range the warm cascade solution is close to the thermodynamic MB distribution and the correction due to finite flux is small. We then perform a qualitative matching of the flux-corrected MB distribution to the compact front, and thereby obtain a relation between ω_{\max} , T and A in (7). To find the warm cascade solution in the inertial range, we consider the Kats–Kontorovich (KK) correction to the Maxwell–Boltzmann distribution:

$$n(\omega) = n_{\text{MB}}(1 + \tilde{n}) = (1 + \tilde{n})Ae^{-\frac{\omega}{T}}, \quad (18)$$

where \tilde{n} is small, $\tilde{n} \ll 1$. By plugging this solution into (15) and linearizing in \tilde{n} we end up with the following ODE- ϵ for the correction

$$\epsilon \omega^{-\frac{13}{2}} A^{-2} e^{\frac{2\omega}{T}} = -S \partial_{\omega\omega} \tilde{n}. \quad (19)$$

3.1.3. Matching

We will now match the KK correction to the front solution. The basic idea is to force the KK solution to satisfy the $n(\omega_{\max}) = 0$ and to have at ω_{\max} the same slope as the front solution. Detailed calculation is presented in Appendix E. The prediction results in:

$$\epsilon = S \omega_{\max}^{\frac{9}{2}} A^2 e^{-\frac{2\omega_{\max}}{T}}. \quad (20)$$

This relation is very important because it gives an analytical relation between the thermodynamic quantities T and A in terms of the energy flux ϵ and the dissipation scale ω_{\max} . However we note that our matching is only qualitative, because the KK correction is supposed to be small which is not the case near the front. Thus, the relation (20) is approximate and we do not expect it to hold precisely.

3.1.4. Alternative approach to find ω_{\max}

Another simple way to find a prediction for the value of ω_{\max} is the following. As we expect to observe a warm cascade, we can ask what will be the range where the thermal component will dominate the dynamics. We can simply assume that in most of the inertial range we will have a distribution $n \simeq n_{\text{MB}}$. Note that the MB distribution always has a positive concavity, $\partial_{\omega\omega} n \geq 0$. On the other hand, we note that our ODE- ϵ can be re-written as

$$\partial_{\omega\omega} n = \frac{1}{n} \left[(\partial_{\omega} n)^2 - \frac{\epsilon}{S \omega^{\frac{13}{2}}} \right], \quad (21)$$

from which it is clear that $\partial_{\omega\omega} n$ may change sign. The point at which $\partial_{\omega\omega} n = 0$ can be considered as s boundary separating the MB range (with negligible flux correction) and the front solution (with large flux correction). This boundary can be estimated by a simple substitution of the MB distribution to the r.h.s. of (21), which gives

$$\epsilon = \frac{A^2 S \omega^{\frac{13}{2}} e^{-\frac{2\omega}{T}}}{T^2} = g_{\epsilon}(\omega, A, T). \quad (22)$$

As this relation contains the exponential factor which decays very fast (for $\omega_{\max} \gg T$, see Appendix E), it is natural to think that the range at which ϵ becomes important appears very sharply and is very near to the point ω_{\max} . Thus, we arrive at the following estimate,

$$\epsilon = \frac{A^2 S \omega_{\max}^{\frac{13}{2}} e^{-\frac{2\omega_{\max}}{T}}}{T^2}. \quad (23)$$

3.2. Constant particle flux: inverse cascade

In analogy to what has been done for the direct cascade, we now look for predictions in the inverse particle cascade η with no flux of

energy. The derivation of the ODE- η that describes such a cascade is straightforward: by integrating equation (11) once and putting $\epsilon = 0$ in (12), we have:

$$\text{constant particles flux} \implies \eta = -\frac{R(\omega, t)}{\omega} = \text{const.} \quad (24)$$

This yields the following Cauchy problem:

$$\begin{cases} \eta = S \omega^{\frac{11}{2}} n^2(\omega) \partial_{\omega\omega} \log n(\omega), \\ n(\omega_0) = n_0, \\ \partial_{\omega} n(\omega_0) = n'_0. \end{cases} \quad (25)$$

This problem is most naturally solved backwards in the ω -space, as we are interested in the inverse cascade. We seek for a solution having a particle flux going from high to low frequencies, i.e. $\eta < 0$ and for convenience we will make the substitution $\eta \rightarrow -|\eta|$ in Eq. (25). The Cauchy problem (25) is very similar to (16) with the only difference in the ω -scaling. Thus we will use the same approach for studying it.

3.2.1. Compact front behavior

Let us find a front solution for the Eq. (24). We now expect the front to be on the left edge of the (inverse cascade) inertial range, i.e. in the vicinity of a certain point $\omega_{\min} < \omega_f$. By plugging $n(\omega) = B(\omega - \omega_{\min})^{\sigma}$ expression into (24) and taking the limit $\omega \rightarrow \omega_{\min}$, in the leading order in $(\omega - \omega_{\min})$ we have:

$$\begin{cases} \sigma = 1 \\ B = \sqrt{\frac{|\eta|}{S \omega_{\min}^{\frac{11}{2}}}} \implies n(\omega) = \sqrt{\frac{|\eta|}{S \omega_{\min}^{\frac{11}{2}}}} (\omega - \omega_{\min}). \end{cases} \quad (26)$$

Thus, the front solution for the inverse particle cascade is also linear in the vicinity of ω_{\min} , with a slope that depends on ω_{\min} and on the value of the particle flux η .

3.2.2. The Kats–Kontorovich correction

As previously supposed for the direct energy cascade, we expect in the most of the inverse-cascade range a corrected thermodynamic spectrum and a front solution behavior at the left end of this range. Let us evaluate the Kats–Kontorovich correction (18), and after that match it to the front solution. By plugging the expression (18) into (24) and linearizing in \tilde{n} we obtain the following ODE- η for the correction,

$$|\eta| \omega^{-\frac{11}{2}} A^{-2} e^{\frac{2\omega}{T}} = -S \partial_{\omega\omega} \tilde{n}. \quad (27)$$

3.2.3. Matching

Again, we want to match the KK correction to the front solution. The idea is very similar to the previously used for the direct cascade, except for the fact that now the limit taken is $\omega_{\min} \ll T$; for details refer to Appendix F. This results in the following condition on the flux,

$$|\eta| = S \left(\frac{9}{2}\right)^2 A^2 \omega_{\min}^{\frac{7}{2}}. \quad (28)$$

3.2.4. Alternative estimate of ω_{\min}

Again, we can obtain an alternative estimate for predicting the range of the warm cascade. Let us rewrite the ODE- η as

$$\partial_{\omega\omega} n = \frac{1}{n} \left[(\partial_{\omega} n)^2 - \frac{|\eta|}{S \omega^{\frac{11}{2}}} \right]. \quad (29)$$

Keeping in mind that the MB distribution is always characterized by a positive concavity, i.e. $\partial_{\omega\omega} n \geq 0$, and considering the

hypothesis $\partial_\omega n \simeq \partial_\omega n_{\text{MB}}$ we find

$$|\eta| = \frac{A^2 S \omega^{\frac{11}{2}} e^{-\frac{2\omega}{T}}}{T^2} = g_\eta(\omega, A, T). \quad (30)$$

Similarly to what we have done for the inverse cascade, we now can suggest that the change of concavity occurs near ω_{\min} . This results in

$$|\eta| = \frac{A^2 S \omega_{\min}^{\frac{11}{2}} e^{-\frac{2\omega_{\min}}{T}}}{T^2}. \quad (31)$$

However, we do not expect a good prediction as before because in this case the exponential term is not a rapidly varying function near ω_{\min} .

3.3. Double cascade

We have now all tools to study the double cascade process. Let us force at ω_f , dissipate at ω_{\max} and ω_{\min} , and consider the case $\omega_{\min} \ll \omega_f \ll \omega_{\max}$. If the forcing range is narrow, the simple relation $\epsilon = \eta \omega_f$ holds for the fluxes. Using this relation, and combining (20) and (28), we can estimate T and A in the system:

$$T = \frac{2\omega_{\max}}{\frac{7}{2} \ln \frac{\omega_{\max}}{\omega_{\min}} + \ln \frac{\omega_{\max}}{\omega_f} - 2 \ln \frac{9}{2}}, \quad (32)$$

$$A = \frac{2}{9} \sqrt{\frac{|\eta|}{S \omega_{\min}^{7/2}}},$$

and, therefore, the chemical potential

$$\mu = T \left(\frac{1}{2} \ln \frac{S \omega_{\min}^{7/2}}{|\eta|} + \ln \frac{9}{2} \right). \quad (33)$$

Note that the temperature appears to be independent of the fluxes and is completely controlled by the forcing and the dissipation scales. This means that increasing the forcing strength without moving ω_f simply adds more particles into the system with the energy per particle remaining the same. The temperature relation (32), up to a constant $-2 \ln(9/2)$ factor, may also be derived by a simple dimensional analysis [39].

4. Numerical results

In this section we present the numerical results obtained by using the DAM and by integrating, at a lower resolution, the HIBE. Our aim is to compare results for the warm cascade solutions of the DAM, which has been devised as a local approximation of the integral collision operator, with direct numerical simulation of the full integro-differential equation (9).

4.1. DAM results

We will first present some numerical experiments on the solution of the Cauchy problems (16) and (25) in which we take for simplicity $S = 1$. Note that all numerical simulations can be performed without any loss of generality starting with a particular value ω_0 because of re-scaling properties described in Appendix G.

4.1.1. Constant direct energy cascade

In Fig. 7 we show the results obtained by integrating equation (16) with $\omega_0 = 3.5$ for different constant energy fluxes ϵ . As initial conditions, we choose the values of the spectrum n_0 and its slope n'_0

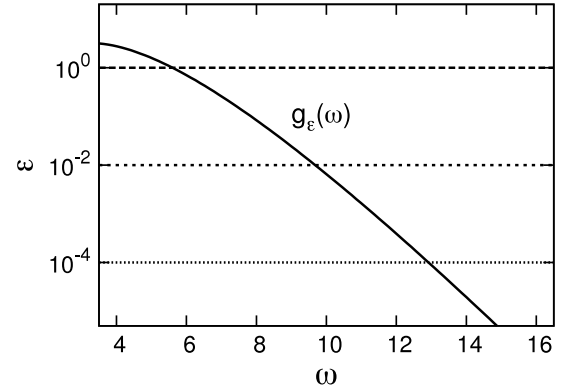


Fig. 8. Plot in the lin-log scale of the function $g_\epsilon(\omega, 1, 1)$, see Eq. (22), which qualitatively defines the thermodynamic regime of the solution.

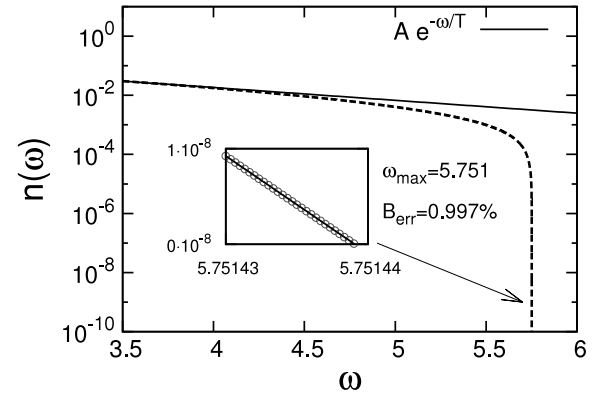


Fig. 9. DAM simulation of ODE- ϵ (16) with constant energy flux $\epsilon = 1$ (dashed line). The initial conditions in $\omega_0 = 3.5$ are set by the MB distribution with $T = 1$ and $A = 1$ (continuous line). The inset shows a zoom of numerical $n(\omega)$ (dots) in the vicinity of the point ω_{\max} where a linear fit is shown by continuous line.

from the MB distribution having $A = 1$ and $T = 1$. The solutions follow the thermodynamic solution (shown as a continuous line) until they rapidly deviate and reach the front in the vicinity of particular values of ω_{\max} . This numerical experiment exhibits two important facts always observed in simulations performed with different initial conditions: the presence of a long transient in which the flux correction is negligible with respect to the thermodynamic MB distribution and the presence of a particular value ω_{\max} at which $n(\omega)$ goes to zero. A lin-log plot of the function $g_\epsilon(\omega, 1, 1)$, see Eq. (22), is shown in Fig. 8: intersection of this curve with horizontal lines at $\epsilon = 1$, $\epsilon = 10^{-2}$ and $\epsilon = 10^{-4}$ marks the predicted cut-off frequencies for the respective flux values. Agreement with the behavior in Fig. 7 is evident: the values of ω_{\max} obtained with Eq. (22) and Fig. 8 coincide with the observed values in Fig. 7 within 5%. Note that the peak of $g_\epsilon(\omega, 1, 1)$ is around $\omega = 3.5$: this is why we set this value as initial condition ω_0 .

In Fig. 9 we present the results for a particular case with flux $\epsilon = 1$. We can appreciate the presence of warm cascade and the front solution near ω_{\max} . The linear behavior of the front is evident in the zoom near ω_{\max} showed in the inset. Numerically we are able to measure ω_{\max} and evaluate B from Eq. (17). The theoretical prediction agrees with the measured slope with the error $B_{\text{err}} = 0.997\%$. The error is evaluated as $B_{\text{err}} = |B_{\text{meas}} - B_{\text{est}}|/B_{\text{meas}}$ where B_{meas} is the measured linear coefficient and B_{est} is the one taken from relation (17). In all other simulations performed with different values of ϵ or different initial conditions, B_{err} is always within 5%.

We now check numerically the validity of the matching prediction (20) by taking different initial condition $n_{\text{MB}}(\omega_0 = 3.5)$ varying T and keeping $A = 1$ and $\epsilon = 1$: results are plotted in Fig. 10.

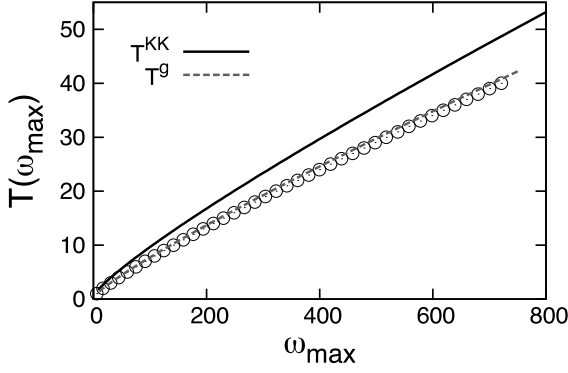


Fig. 10. Checking of predictions in the DAM constant energy flux cascade (16): the points represent the temperature of the initial condition T with respect to the measured ω_{\max} . The solid line is the matching relation (20) while the dashed one is obtained from (23).

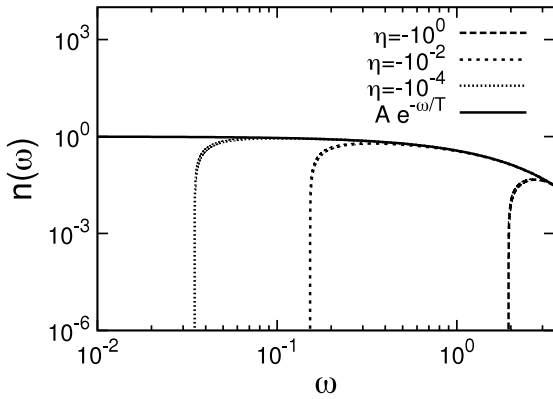


Fig. 11. The DAM simulations of (25) for different constant inverse particle flux η starting with the same initial condition at $\omega_0 = 3.5$ given by the Boltzmann distribution $n_{\text{MB}}(\omega) = Ae^{-\omega/T}$, where $A = 1$ and $T = 1$ (plotted with continuous line).

It is evident from the figure that the predicted temperature (continuous black line) evaluated from relation (20) is an overestimation of the numerical results (dots) and the error is around 10%. Finally, the prediction for the alternative temperature relation (23) is plotted with gray dashed line: it appears to give a better estimation than relation (20).

4.1.2. Constant particle cascade

We now investigate the inverse particle cascade by solving Cauchy problem (25). In Fig. 11 we show numerical results obtained by taking initial conditions at ω_0 from the MB distribution $n_{\text{MB}}(\omega) = Ae^{-\omega/T}$ with $T = 1$, $A = 1$. As in the case of constant energy flux, here the warm cascade range is wider for smaller flux values. We also observe the fronts in vicinities of the cutoff point ω_{\min} . In Fig. 12 we show the function $g_\eta(\omega, 1, 1)$ which represents the prediction of the thermodynamic range (30). Results in Fig. 11 show poor agreement with this naïve estimation.

The front solution is analyzed in detail in Fig. 13 where we choose the particular case with $\eta = -1$. The linear behavior is demonstrated in the inset. Moreover, a numerical estimation of ω_{\min} allows us to evaluate B , see Eq. (26). The error B_{err} is presented in the figure; for all other simulations we have performed, B_{err} remained within 4%.

Finally we check KK matching prediction for the thermodynamic quantity A with respect to ω_{\min} presented in Eq. (28): results are showed in Fig. 14. In this case the KK analytical prediction (continuous line) underestimates the numerical data while the estimation (31) is completely out of range (dashed line). However,

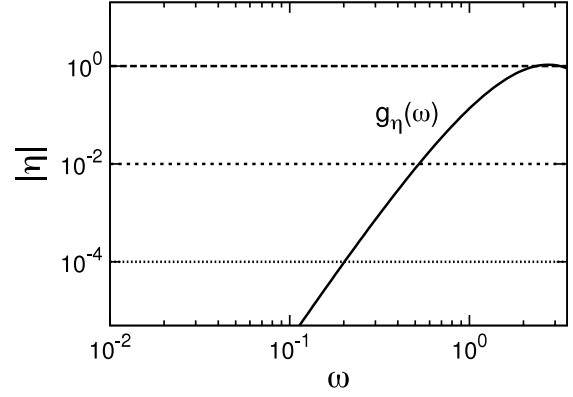


Fig. 12. Plot of the function $g_\eta(\omega, 1, 1)$, see Eq. (30).

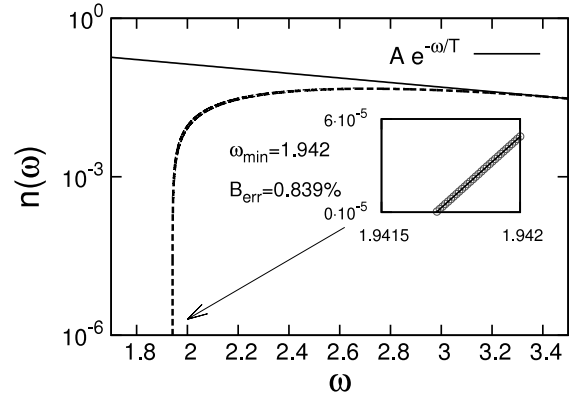


Fig. 13. The DAM simulation of (25) with $\eta = -1$ (dashed line) starting with initial condition at $\omega_0 = 3.5$ given by the MB distribution $n_{\text{MB}}(\omega) = Ae^{-\omega/T}$ where $A = 1$ and $T = 1$ (plotted with continuous line). Inset: lin–lin scale zoom in the vicinity ω_{\min} (dots) where the best linear fit is presented with a continuous line.

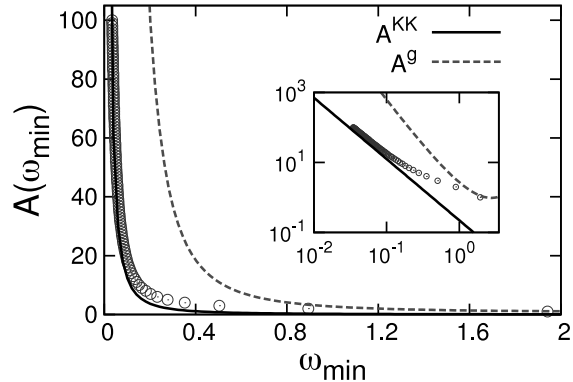


Fig. 14. Checking predictions in the DAM constant inverse flux cascade (25): the points represent the thermodynamic quantity A with respect to the measured ω_{\min} . The continuous line is the KK matching prediction given in Eq. (28) while the dashed one is obtained from (31).

the scaling $A \sim \omega_{\min}^{-7/4}$ of KK prediction tends to be reached for small values of ω_{\min} , where $\omega_{\min} \ll T$.

4.1.3. Double cascade

An example of double cascade is presented in Fig. 15 where we set the forcing at $\omega_f = \omega_0 = 3.5$. We show here three cases where the particle fluxes are respectively $\eta = -1$, $\eta = -10^{-2}$ and $\eta = -10^{-4}$. Measuring ω_{\min} and ω_{\max} for each case we are able to estimate the temperature T_{est} from prediction (32). Results do not agree with the expected temperature (the initial conditions set it at $T = 1$) but they approach this value for bigger ranges, i.e.

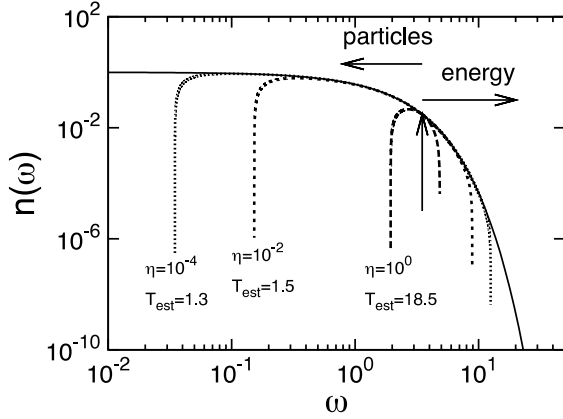


Fig. 15. The DAM double cascade simulations of Eqs. (16) and (25) for three different values of the particle flux η (and consequently of the energy flux $\epsilon = \eta\omega_f$). The initial condition are taken at $\omega_f = 3.5$ from the MB distribution with $T = 1$ and $A = 1$. Measuring ω_{\min} and ω_{\max} in each case, we estimate of the temperature T_{est} from prediction (32).

when the condition $\omega_{\min} \ll \omega_f \ll \omega_{\max}$ is better satisfied (see for example the case $\eta = -10^{-4}$).

4.2. HIBE results

We now present results of the direct simulation of the HIBE with the exact Boltzmann collision integral and compare them with predictions obtained with the DAM. As we have mentioned, the evaluation of (4) is numerically challenging and it is nowadays practically impossible to simulate such wide ω -space range as we have done using the DAM. In the present work, we have discretized the ω space using 101 grid points with $\omega \in [0, \omega_{\text{cutoff}}]$ and the resolution considered is $\Delta\omega = \frac{\omega_{\text{cutoff}}}{100}$. We have checked that the numerical simulations are mesh independent by taking 201 points. Before describing the numerical results, in the following paragraph we briefly explain the numerical scheme which has been adopted.

The difficulty of solving numerically the forced-dissipated HIBE (9) comes from the evaluation of the collision integral I_{coll} which is defined in (4). The three dimensional integral must be calculated only within the resonant manifold defined by the δ -function. Numerically, the set of points that satisfy the resonant conditions $\mathcal{M} = \{\omega_1, \omega_2, \omega_3, \omega_4\} / \omega_1 + \omega_2 = \omega_3 + \omega_4$ are pre-computed. Because of the presence of the dissipation, the integration limits are $\omega = 0$ and $\omega = \omega_{\text{cutoff}}$, where $\omega_{\text{cutoff}} \geq 2\omega_{\max}$ in order to prevent ultraviolet bottleneck effect. The integral is performed by using the trapezoid rule. Finally, the time evolution of (4) is obtained by applying the Euler scheme where the collision integral, the dissipation and the forcing are those resulting from the previous time step. We underline that Boltzmann collision integral is computed without using any stochastic technique like Monte Carlo methods. Further details on numerical methods for solving the HIBE and a simple code can be found in [40].

4.2.1. Direct cascade study

We first analyze the direct energy cascade by putting the forcing scale near the low- ω dissipation scale in order to have a wider direct inertial range. Numerical results for these final steady states were previously presented as examples in Figs. 2 and 4. We concentrate now only on the last one: here we kept fixed $\omega_{\min} = 5$, $\omega_f = 21$ and $\omega_{\max} = 95$ and varied the forcing coefficient, i.e. the fluxes η and ϵ . We claimed that the temperature of the systems is the same because qualitatively the distributions have identical slopes. Moreover, we observed in all the examples that the left and right branch chemical potentials and temperatures can be defined by the forcing scale.

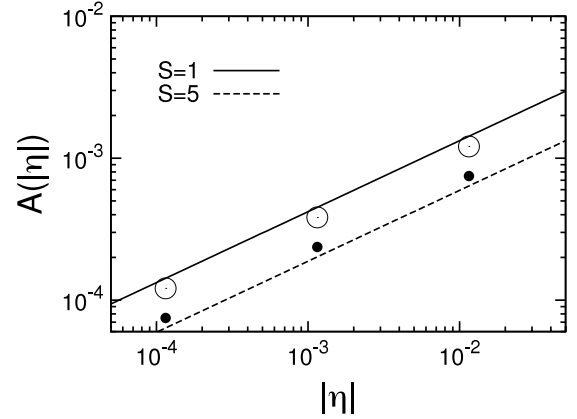


Fig. 16. Results for the fitted values of the thermodynamic quantity $A = e^{-\frac{\epsilon}{T}}$ plotted against the forcing levels, as obtained in the simulations shown in Fig. 4: the values of A_L are shown by filled circles while A_R by empty ones. The continuous and dashed lines refer to prediction (32) with $S = 1$ and $S = 5$ respectively.

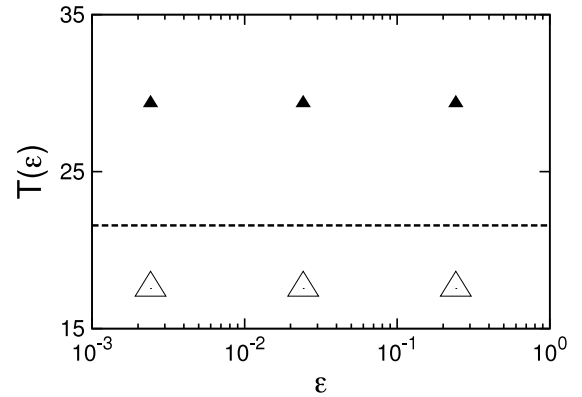


Fig. 17. Measured temperatures T_L (filled triangles) and T_R (empty ones) obtained in the simulations shown in Fig. 4. The dashed line is the analytical prediction (32).

Having in mind the DAM results, we have measured A and T in three examples presented in Fig. 4: the results are shown in Fig. 16 and are compared to analytical predictions (32). As expected the quantity $A \sim \sqrt{\eta}$ and two lines, in log-log coordinates, are drawn from prediction (32) taking different values of the constant S in order to match the interval between A_L and A_R , represented with filled and empty circles, respectively. Here we have chosen $S = 1$ and $S = 5$ for continuous and dashed line, respectively. The temperature is shown in Fig. 17: even though T_L and T_R are different they both appear to be forcing independent, as predicted. The temperature is evaluated from relation (32): temperature (dashed line) stands in between these values, and closer to T_R , which, again, is natural because the right inertial interval is wider.

We have also analyzed the sensitivity of the temperature to changes of the high- ω dissipation range; results are presented in Fig. 18. Keeping the forcing constant and changing the value of ω_{\max} the system reaches steady states characterized by different temperatures T_L (filled circles) and T_R (empty circles). The prediction (32), shown by the continuous line, is in between the two temperatures and is closer to T_R —again due to the wider right range.

4.2.2. Inverse cascade study

Finally, we have performed some simulations by setting the forcing scale near the dissipation at high ω 's in order to study the inverse cascade process. In this case too, as reported in Fig. 3, we observe two different values of thermodynamic quantities on the left and on the right of the forcing. Here, we are able to study the

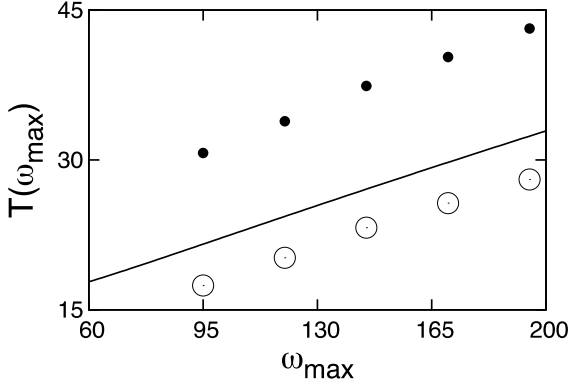


Fig. 18. Temperature in different steady state keeping the forcing constant and varying the dissipation scale ω_{\max} : big empty circles correspond to the temperature T_R on the right of the forcing scale, whereas small filled circles to the left side, T_L . The continuous line is the prediction (32).

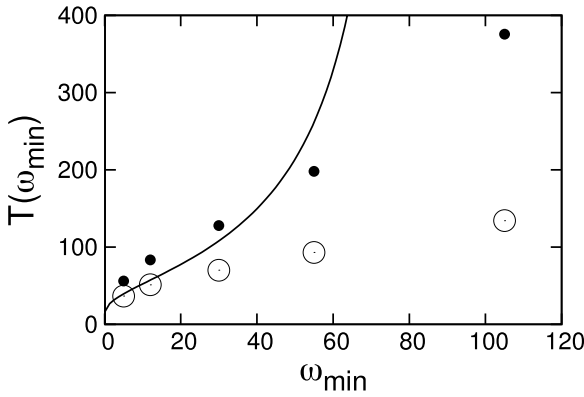


Fig. 19. Temperature in different steady state keeping the forcing constant and varying the dissipation scale ω_{\min} : big empty circles correspond to the temperature T_R on the right of the forcing scale, whereas small filled circles to the left side, T_L . The continuous line is the prediction (32).

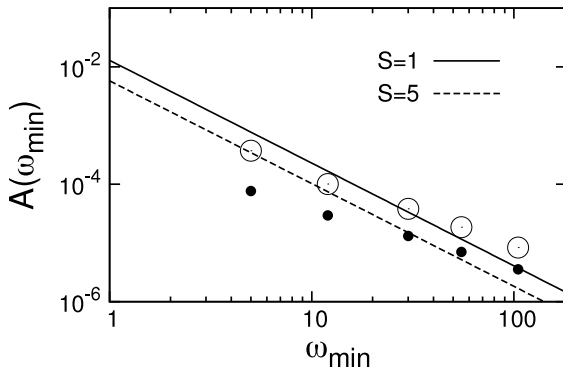


Fig. 20. Thermodynamic amplitude A for different ω_{\min} and fixed forcing in log–log scales in numerical simulations of the HIBE. Filled circles corresponds to A_L while empty circles to A_R . The continuous and dashed lines are formula (32) with $S = 1$ and $S = 5$ respectively.

scaling of the thermodynamic quantities T and A with respect to changes of the small- ω dissipation scale ω_{\min} . Results for T are shown in Fig. 19 and for A in Fig. 20, with the “left” quantities shown by filled circles and the “right” ones by empty circles. There is a reasonably good agreement of T with the prediction (32) for small ω_{\min} . This is natural because smaller ω_{\min} corresponds to a larger inverse cascade inertial range and also because the prediction is valid when $\omega_{\min} \ll T$.

On the other hand, for A the prediction (32) in the range obtained choosing the interval with $S = 1$ and $S = 5$ as in

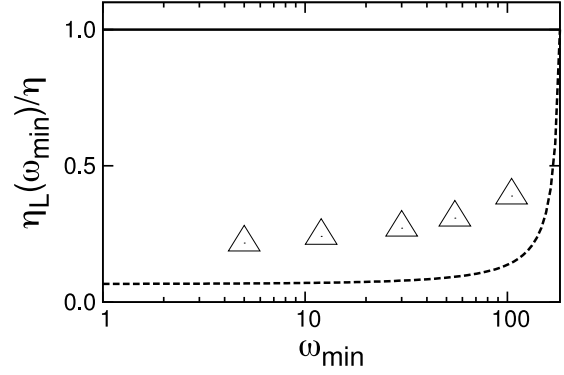


Fig. 21. The plot shows in the log-linear scale the ratio of the measured inverse particle flux over the total one η_L/η (empty triangles) with respect to ω_{\min} ; the continuous line correspond to the total flux while the dashed one follows the finite range correction (34).

Fig. 16 does not match so well the numerical results. However, we can make the two following comments. First, we underline that the agreement with the $A \sim \omega_{\min}^{-7/2}$ behavior becomes much more evident for small values of ω_{\min} . This is natural because the prediction has been derived in the limit $\omega_{\min} \ll \omega_f$ and $\omega_{\min} \ll T$. Second, the particle flux which defines A in relation (32) can be smaller due to finite range effects. Indeed, following [41], the ratio of the leftward particle flux to the total particle production rate is estimated as:

$$\eta_L = \eta \frac{\omega_{\max} - \omega_f}{\omega_{\max} - \omega_{\min}}. \quad (34)$$

This equation states that for the particle flux to be mostly to the left, both inertial ranges must be large (note that this is also the condition of validity of the Fjørtoft argument). Fig. 21 shows the behavior of the normalized left measured flux η_L/η (empty triangles) with respect to ω_{\min} . We can clearly see that the measured particle flux is indeed much smaller than the one imposed by the forcing term (continuous line), around one third of it. This is in quite good agreement with the finite range prediction (34) plotted with dashed line. Similar reasoning can be made for corrections on $A(|\eta|)$ in the case of the direct cascade example in Fig. 16.

5. Conclusions

In the present paper we have investigated stationary turbulent states in the isotropic Boltzmann kinetic equation for hard spheres. This was done by looking for steady nonequilibrium states in open systems, that is when forcing and dissipation mechanisms are present. Analogies with similar results of wave turbulence theory suggest the manifestation of a *warm cascade*, i.e. a constant direct flux of energy and inverse flux of particles on background of thermodynamic Maxwell–Boltzmann distribution. This is a consequence of opposite flux directions in KZ solutions with respect to the Fjørtoft argument predictions.

We have built an ad-hoc differential approximation model to easily simulate the cascade processes. Indeed, this simplification allowed us to reach a wide range of scales inaccessible by solving the isotropic Boltzmann kinetic equation directly. Simulations show the presence of a warm cascade with approximately the MB shape followed by a sharp front for both energy and particle cascades. We have physically interpreted ω_{\min} and ω_{\max} as intrinsic dissipation scales at low and high ω 's which are necessary to establish the steady state. Moreover, we have found analytical predictions relating the particle and energy fluxes, forcing and dissipations scales to the thermodynamic quantities of the system.

In particular, we have shown that the temperature is independent of the amplitude of the fluxes but only depends on the forcing and dissipation scales.

We have then compared the theoretical predictions and the numerical results obtained with the differential approximation model with simulations of the complete isotropic Boltzmann kinetic equation. Even though the resolution for the latter was limited by the available computational power, the results are comparable and in good agreement with the analytical predictions. In particular we have verified that the steady state is characterized by a warm cascade where a fitted thermodynamic Maxwell–Boltzmann distribution has been used to measure temperature and chemical potential of the system. We observe, in agreement with our analytical predictions, that the temperature is completely defined by the forcing and dissipation scales and does not depend on the fluxes.

We hope that this work may open some perspectives toward understanding nonequilibrium steady states and their net currents (fluxes) by cross-fertilization with the weak turbulence theory.

Acknowledgments

We would like to thank Guido Boffetta, Colm Connaughton, Filippo De Lillo, Stefano Musacchio, Al Osborne, and Arturo Viero for fruitful discussions. Simulations were performed on computational resources founded by the Office of Naval Research (ONR). Finally, we are grateful to the Gnu Scientific Library (GSL) developers for providing free software which has been used for simulations.

Appendix A. Different notation of the Boltzmann collision integral

The Boltzmann collision integral can be written in different forms depending on the choice of the integration variables. In many classical books the collision integral has the following form (see for example Eqs. (3–55) in [42]):

$$I_{\text{coll}} = \frac{1}{m} \int \sigma(\chi, V) V (n_3 n_4 - n_1 n_2) d\mathbf{v}_2 d\Omega, \quad (\text{A.1})$$

where m is the mass of the identical particles, $V = \mathbf{v}_2 - \mathbf{v}_1$ is the relative velocity of the particles before the collision, $\sigma(\chi, V)$ is the collision cross section and $d\Omega = \sin(\chi) d\chi d\epsilon$, i.e. the differential solid angle at the deflection angle χ . In what follows we will show that the form of the collision integral reported in Eq. (2) is the same as the one in Eq. (A.1).

In our notation the particle momentum is defined as $\mathbf{k}_i = m\mathbf{v}_i$. We start from the collision integral presented in Eq. (2)

$$I_{\text{coll}} = \int_{-\infty}^{+\infty} W_{12}^{34} [n(\mathbf{x}, \mathbf{k}_3, t) n(\mathbf{x}, \mathbf{k}_4, t) - n(\mathbf{x}, \mathbf{k}_1, t) n(\mathbf{x}, \mathbf{k}_2, t)] d\mathbf{k}_2 d\mathbf{k}_3 d\mathbf{k}_4, \quad (\text{A.2})$$

and perform the following change of variables:

$$\begin{cases} \mathbf{P} = \frac{\mathbf{k}_1 + \mathbf{k}_2 - \mathbf{k}_3 - \mathbf{k}_4}{m} \\ \mathbf{V} = \frac{\mathbf{k}_2 - \mathbf{k}_1}{m} \\ \mathbf{V}' = \frac{\mathbf{k}_4 - \mathbf{k}_3}{m} \end{cases} \quad \Leftrightarrow \quad \begin{cases} \mathbf{k}_2 = m(\mathbf{V} + \mathbf{v}_1) \\ \mathbf{k}_3 = \frac{m}{2}(\mathbf{V} - \mathbf{V}' - \mathbf{P} + 2\mathbf{v}_1) \\ \mathbf{k}_4 = \frac{m}{2}(\mathbf{V} + \mathbf{V}' - \mathbf{P} + 2\mathbf{v}_1) \end{cases} \quad (\text{A.3})$$

It is straightforward to check that the Jacobian of the transformation is $m^3/2$. The collision integral results in:

$$I_{\text{coll}} = \frac{m^3}{2} \int \Gamma(\mathbf{P}, \mathbf{V}, \mathbf{V}') (n_3 n_4 - n_1 n_2) \times \delta(m\mathbf{P}) \delta\left(\frac{m^2 [V^2 - V'^2 + 2\mathbf{P} \cdot (\mathbf{V} + 2\mathbf{v}_1) - P^2]}{2}\right) \times d\mathbf{P} d\mathbf{V} d\mathbf{V}'. \quad (\text{A.4})$$

Using the properties of the δ functions and introducing spherical coordinates for vector \mathbf{V}' we get:

$$I_{\text{coll}} = \frac{1}{m} \int \frac{m}{2} \Gamma(\mathbf{V}, \chi) V (n_3 n_4 - n_1 n_2) d\mathbf{V} d\Omega, \quad (\text{A.5})$$

with $d\Omega = \sin \chi d\chi d\epsilon$. Comparing this last equivalence with Eq. (A.1) it holds $\sigma(\mathbf{V}, \chi) = \frac{m}{2} \Gamma(\mathbf{V}, \chi)$.

Appendix B. Three-dimensional δ -function angular average

The angular average of the four-wave linear momentum conservation $\delta(\mathbf{k}_{12}^{34}) = \delta(\mathbf{k}_1 + \mathbf{k}_2 - \mathbf{k}_3 - \mathbf{k}_4)$ is evaluated by splitting it into two δ -functions of three particle collision. This results in

$$\begin{aligned} & \int_{\Omega} \delta(\mathbf{k}_{12}^{34}) d\Omega_{1234} \\ &= \int_{\Omega} \int_{\mathbf{k}_{\min}}^{\mathbf{k}_{\max}} \delta(\mathbf{k}_1 + \mathbf{k}_2 - \mathbf{k}) \delta(\mathbf{k}_3 + \mathbf{k}_4 - \mathbf{k}) d\mathbf{k} d\Omega_{1234} \\ &= \int_{\mathbf{k}_{\min}}^{\mathbf{k}_{\max}} \left[\int_{\Omega} \delta(\mathbf{k}_1 + \mathbf{k}_2 - \mathbf{k}) d\Omega_{12} \right] \\ & \quad \times \left[\int_{\Omega} \delta(\mathbf{k}_3 + \mathbf{k}_4 - \mathbf{k}) d\Omega_{34} \right] k^{d-1} d\mathbf{k} d\Omega \\ &= 4\pi \int_{\mathbf{k}_{\min}}^{\mathbf{k}_{\max}} \frac{1}{2kk_1k_2} \frac{1}{2kk_3k_4} k^2 d\mathbf{k} \\ &= \frac{2\pi}{k_1 k_2 k_3 k_4} \min(k_1, k_2, k_3, k_4), \end{aligned} \quad (\text{B.1})$$

where geometrically $k_{\min} = |k_1 - k_2| = |k_3 - k_4|$ and $k_{\max} = k_1 + k_2 = k_3 + k_4$. For details about the integration of three particle δ -function see Appendices in [5].

Appendix C. The Kolmogorov–Zakharov solutions for the general HIBE

The Boltzmann collision integral I_{coll} is defined as

$$I_{\text{coll}}(\mathbf{x}, \mathbf{k}_1, t) = \int_{-\infty}^{\infty} \Gamma_{12}^{34} [n(\mathbf{x}, \mathbf{k}_3, t) n(\mathbf{x}, \mathbf{k}_4, t) - n(\mathbf{x}, \mathbf{k}_1, t) n(\mathbf{x}, \mathbf{k}_2, t)] \times \delta(\mathbf{k}_1 + \mathbf{k}_2 - \mathbf{k}_3 - \mathbf{k}_1) \delta(|\mathbf{k}_1|^2 + |\mathbf{k}_2|^2 - |\mathbf{k}_3|^2 - |\mathbf{k}_4|^2) d\mathbf{k}_{234}, \quad (\text{C.1})$$

where the two δ -functions assure the conservation of the linear momentum and kinetic energy. In the isotropic case it is convenient to move in the energy domain $\omega_i = |\mathbf{k}_i|^2 \in [0, +\infty)$ and so the HIBE results in

$$I(\omega_1) = \int_0^{\infty} S_{12}^{34} (n_3 n_4 - n_1 n_2) \delta(\omega_{12}^{34}) d\omega_{234}, \quad (\text{C.2})$$

where $I(\omega_1) = \int_{\Omega} I_{\text{coll}}(\mathbf{x}, \omega_1, t) \omega_1^{\frac{d-1}{2}} \left| \frac{d\mathbf{k}_1}{d\omega_1} \right|$ and we use for brevity

$n_i = n(\omega_i) = n(\mathbf{x}, |\mathbf{k}_i|^2, t)$, and $\delta(\omega_{12}^{34}) = \delta(\omega_1 + \omega_2 - \omega_3 - \omega_4)$. The functional S is

$$S_{12}^{34} = \frac{1}{16} (\omega_1 \omega_2 \omega_3 \omega_4)^{\frac{d}{2}-1} \langle \Gamma_{12}^{34} \delta(\mathbf{k}_1 + \mathbf{k}_2 - \mathbf{k}_3 - \mathbf{k}_4) \rangle_{\Omega} \quad (\text{C.3})$$

and the operator $\langle \cdot \rangle_{\Omega}$ states for the integration over solid angles. It is important for the following to estimate the homogeneity degree of S . Supposing that the collisional kernel scales as $\Gamma_{\lambda(12)}^{\lambda(34)} = \lambda^{2\beta} \Gamma_{12}^{34}$, we have

$$S_{\lambda(12)}^{\lambda(34)} = \lambda^{4\left(\frac{d}{2}-1\right)+2\beta-\frac{d}{2}} S_{12}^{34} = \lambda^{\frac{3d}{2}+2\beta-4} S_{12}^{34}. \quad (\text{C.4})$$

Moreover, its behavior at the boundaries of integration is

$$\lim_{\omega_i \rightarrow +\infty} S_{12}^{34} \sim \omega_i^{d-2+\tau_1} \quad (\text{C.5})$$

$$\lim_{\omega_i \rightarrow 0^+} S_{12}^{34} \sim \omega_i^{\frac{d}{2}-1+\tau_2}$$

if we assume that

$$\lim_{\omega_i \rightarrow +\infty} \langle \Gamma_{12}^{34} \delta(\mathbf{k}_1 + \mathbf{k}_2 - \mathbf{k}_3 - \mathbf{k}_4) \rangle_{\Omega} \sim \omega_i^{\tau_1} \quad (\text{C.6})$$

and

$$\lim_{\omega_i \rightarrow 0^+} \langle \Gamma_{12}^{34} \delta(\mathbf{k}_1 + \mathbf{k}_2 - \mathbf{k}_3 - \mathbf{k}_4) \rangle_{\Omega} \sim \omega_i^{\tau_2} \quad (\text{C.7})$$

(note that for $\omega_i \rightarrow \infty$ also another ω_j must go to infinity due to the δ -function).

In the following we will suppose that the particle distribution function follows the power-law distribution $n(\omega) = A\omega^{-\nu}$ and so

$$I(\omega_1) = A^2 \int_0^\infty S_{1(3+4-1)}^{34} [\omega_3^{-\nu} \omega_4^{-\nu} - \omega_1^{-\nu} (\omega_3 + \omega_4 - \omega_1)^{-\nu}] \Theta(\omega_3 + \omega_4 - \omega_1) d\omega_3 d\omega_4, \quad (\text{C.8})$$

where Θ is the Heaviside step function.

C.1. The Kolmogorov–Zakharov solutions

We will present the Kolmogorov–Zakharov solutions of the collision integral using the method presented by Balk in [25]. The collision integral, without any loss of generality, can be rewritten as

$$I(\omega_1) = A^2 \omega_1^{-1-\mu} \int_0^\infty S_{12}^{34} (\omega_3^{-\nu} \omega_4^{-\nu} - \omega_1^{-\nu} \omega_2^{-\nu}) \times (\omega_1 \omega_2 \omega_3 \omega_4) \omega_1^\mu \delta(\omega_{12}^{34}) \frac{d\omega_2}{\omega_2} \frac{d\omega_3}{\omega_3} \frac{d\omega_4}{\omega_4} \quad (\text{C.9})$$

where the exponent

$$\mu = 2\nu + 1 - 2\beta - \frac{3d}{2} \quad (\text{C.10})$$

is chosen in order to have zero as homogeneity coefficient of the integrand (excluding the differentials $\frac{d\omega_i}{\omega_i}$). If the integral converges, Balk proved that is possible to interchange the three integration index in the integrand with the fourth one, ω_1 . Thanks to the symmetric properties of the collision kernel we can write

$$I(\omega_1) = \frac{A^2 \omega_1^{-1-\mu}}{4} \int_0^\infty S_{12}^{34} (\omega_3^{-\nu} \omega_4^{-\nu} - \omega_1^{-\nu} \omega_2^{-\nu}) (\omega_1 \omega_2 \omega_3 \omega_4) \times (\omega_1^\mu + \omega_2^\mu - \omega_3^\mu - \omega_4^\mu) \delta(\omega_{12}^{34}) \frac{d\omega_2}{\omega_2} \frac{d\omega_3}{\omega_3} \frac{d\omega_4}{\omega_4}, \quad (\text{C.11})$$

which clearly vanishes for $\mu = 0$ or $\mu = 1$. This corresponds to the condition on the exponent

$$\nu_0 = \nu|_{\mu=0} = \frac{3d-2}{4} + \beta \quad (\text{C.12})$$

$$\nu_1 = \nu|_{\mu=1} = \frac{3d}{4} + \beta.$$

Note that first KZ solution for the HIBE were presented in [17].

C.2. Convergence of the integral (locality condition)

The locality of interactions is guaranteed by the convergence of the collision integral. We then investigate the possible values of ν which assure the convergence around the integrand singularities.

C.2.1. Limit $\omega_3 \rightarrow \infty$

In the limit of $\omega_3 \rightarrow \infty$ we can approximate $(\omega_3 + \omega_4 - \omega_1)^{-\nu} = \omega_3^{-\nu} - \nu \omega_3^{-\nu-1} (\omega_4 - \omega_1) + O(\omega_3^{-\nu-2})$ at the second order. The argument in the square brackets of (C.8) results in

$$[\dots] \simeq \omega_3^{-\nu} [\omega_4^{-\nu} - \omega_1^{-\nu} + \nu \omega_1^{-\nu} \omega_3^{-1} (\omega_4 - \omega_1)]. \quad (\text{C.13})$$

As a consequence, when $\nu > 0$, the integrand for large ω_3 goes like $\frac{\omega_4^{-\nu} - \omega_1^{-\nu}}{\omega_3^{d-2+\tau_1}}$ and so the convergence condition is

$$\nu > d - 1 + \tau_1. \quad (\text{C.14})$$

C.2.2. Limit $\omega_3 \rightarrow 0^+$

In the limit of $\omega_3 \rightarrow 0^+$ we can approximate $(\omega_3 + \omega_4 - \omega_1)^{-\nu} = (\omega_4 - \omega_1)^{-\nu} - \nu \omega_3 (\omega_4 - \omega_1)^{-\nu-1} + O(\omega_3^2)$ at the second order. The argument in the square brackets of (C.8) results in

$$[\dots] = \omega_3^{-\nu} [\omega_4^{-\nu} - \omega_1^{-\nu} \omega_3^\nu (\omega_4 - \omega_1)^{-\nu} + \nu \omega_1^{-\nu} \omega_3^{\nu+1} (\omega_4 - \omega_1)^{-\nu-1}]. \quad (\text{C.15})$$

Therefore, when $\nu > 0$, the integrand for small ω_3 goes like $\frac{\omega_4^{-\nu}}{\omega_3^{\nu-\frac{d}{2}+1-\tau_2}}$ and the convergence condition is

$$\nu < \frac{d}{2} + \tau_2. \quad (\text{C.16})$$

An analogue condition holds for the singularity $(\omega_3 + \omega_4 - \omega_1)^{-\nu} \rightarrow 0^+$.

C.3. Constant fluxes

The solutions $n(\omega) = A\omega^{-\nu_0}$ and $n(\omega) = A\omega^{-\nu_1}$ correspond to a constant flux of particle and energy, respectively. To demonstrate this fact we perform the substitution $\omega_i = \omega_1 \xi_i \forall i \neq 1$ in the Eq. (C.11) which results, recalling the homogeneity of the integrand function, in

$$I(\omega_1) = \frac{A^2 \omega_1^{-1-\mu}}{4} \int_{\Delta} S_{1\xi_2}^{\xi_3 \xi_4} (\xi_3^{-\nu} \xi_4^{-\nu} - \xi_2^{-\nu}) (\xi_2 \xi_3 \xi_4) \times (1 + \xi_2^\mu - \xi_3^\mu - \xi_4^\mu) \delta(1 + \xi_2 - \xi_3 - \xi_4) d\xi_{234} = \frac{A^2 \omega_1^{-1-\mu}}{4} U(\mu). \quad (\text{C.17})$$

The integral $U(\mu)$ is now performed over the triangle Δ in the $\xi_3 \times \xi_4$ space satisfying the conditions $0 \leq \xi_i \leq 1$ and $\xi_4 \geq 1 - \xi_3$, without any dependence on ω_1 .

C.3.1. Flux of particles

The flux of particles is defined as

$$Q(\omega) = - \int_0^\omega I(\omega_1) d\omega_1 = - \frac{A^2 U(\mu)}{4} \int_0^\omega \omega_1^{-1-\mu} d\omega_1 = \frac{A^2 U(\mu) \omega^{-\mu}}{4\mu}. \quad (\text{C.18})$$

If $\mu = 1$ the flux is zero while in the case $\mu = 0$ it is indeterminate. By applying the De l'Hôpital rule in the latter case we find

$$Q(\omega)|_{\mu=0} = \frac{A^2}{4} \int_{\Delta} S_{1\xi_2}^{\xi_3 \xi_4} (\xi_3^{-\nu_0} \xi_4^{-\nu_0} - \xi_2^{-\nu_0}) (\xi_2 \xi_3 \xi_4) \ln \left(\frac{\xi_2}{\xi_3 \xi_4} \right) \times \delta(1 + \xi_2 - \xi_3 - \xi_4) d\xi_{234}. \quad (\text{C.19})$$

The integrand, and consequently the sign of the particle flux, is always negative for $\nu_0 > 0$. This is clear by looking at the sign of every factors in the integral: all are trivially positive except $(\xi_3^{-\nu_0} \xi_4^{-\nu_0} - \xi_2^{-\nu_0})$ and $\ln\left(\frac{\xi_2}{\xi_3 \xi_4}\right)$. Recalling that $(1 - \xi_3)(1 - \xi_4) \geq 0$ and $\xi_2 = \xi_3 + \xi_4 - 1$, we have

$$\begin{aligned} 0 &\leq (1 - \xi_3)(1 - \xi_4) = \xi_3 \xi_4 - \xi_3 - \xi_4 + 1 \\ &= \xi_3 \xi_4 - \xi_2 \implies \xi_3 \xi_4 \geq \xi_2, \end{aligned} \quad (\text{C.20})$$

which leads to $\ln\left(\frac{\xi_2}{\xi_3 \xi_4}\right) \leq 0$ and $(\xi_3^{-\nu_0} \xi_4^{-\nu_0} - \xi_2^{-\nu_0}) \leq 0$ (for positive ν_0). As a consequence $Q(\omega) \geq 0$, that is the particle flux goes from low to high frequencies.

C.3.2. Flux of energy

The flux of energy is

$$\begin{aligned} P(\omega) &= - \int_0^\omega I(\omega_1) \omega_1 d\omega_1 \\ &= - \frac{A^2 U(\mu)}{4} \int_0^\omega \omega_1^{-\mu} d\omega_1 = - \frac{A^2 U(\mu) \omega_1^{1-\mu}}{4(1-\mu)} \end{aligned} \quad (\text{C.21})$$

and is null when $\mu = 0$ while indeterminate in the case $\mu = 1$. Again applying the De l'Hôpital rule we have

$$\begin{aligned} P(\omega)|_{\mu=1} &= \frac{A^2}{4} \int_{\Delta} S_{12}^{\xi_3 \xi_4} (\xi_3^{-\nu_1} \xi_4^{-\nu_1} - \xi_2^{-\nu_1}) (\xi_2 \xi_3 \xi_4) \\ &\quad \times [\xi_2 \ln(\xi_2) - \xi_3 \ln(\xi_3) - \xi_4 \ln(\xi_4)] \\ &\quad \times \delta(1 + \xi_2 - \xi_3 - \xi_4) d\xi_{234}. \end{aligned} \quad (\text{C.22})$$

As previously discussed, the term $(\xi_3^{-\nu_1} \xi_4^{-\nu_1} - \xi_2^{-\nu_1}) \leq 0$ for every $\nu_1 > 0$. Differently, the factor $[\xi_2 \ln(\xi_2) - \xi_3 \ln(\xi_3) - \xi_4 \ln(\xi_4)]$ is always positive but here the demonstration is not so trivial as in the previous case and for a complete discussion see [18]. $P(\omega) \leq 0$, which means that the energy flux goes from high to low frequencies.

Appendix D. The DAM for the homogeneous isotropic Boltzmann equation

The homogeneous isotropic Boltzmann equation (4) in ω -space is

$$\frac{\partial N_1}{\partial t} = \int S_{12}^{34} (n_3 n_4 - n_1 n_2) \delta(\omega_1 + \omega_2 - \omega_3 - \omega_4) d\omega_{234}, \quad (\text{D.1})$$

where for the hard sphere model

$$S_{12}^{34} = 2\pi \min[\sqrt{\omega_1}, \sqrt{\omega_2}, \sqrt{\omega_3}, \sqrt{\omega_4}]. \quad (\text{D.2})$$

For every smooth function $g(\omega_i)$ the following equality holds

$$\begin{aligned} &\int \frac{\partial N_1}{\partial t} g(\omega_1) d\omega_1 \\ &= \int S_{12}^{34} (n_3 n_4 - n_1 n_2) \delta(\omega_1 + \omega_2 - \omega_3 - \omega_4) g(\omega_1) d\omega_{1234} \\ &= \frac{1}{4} \int S_{12}^{34} (n_3 n_4 - n_1 n_2) \delta(\omega_1 + \omega_2 - \omega_3 - \omega_4) \\ &\quad \times [g(\omega_1) + g(\omega_2) - g(\omega_3) - g(\omega_4)] d\omega_{1234}, \end{aligned} \quad (\text{D.3})$$

due to the symmetry properties of the integrand.

If the interactions are local, i.e. during the collision $\omega_1 \simeq \omega_2 \simeq \omega_3 \simeq \omega_4$, then one can write that $\omega_i = \omega_1 + \Delta_i$ for $i = 2, 3, 4$, with $\Delta_i \ll \omega_1$. The δ -function, solved in ω_3 , implies that

$\omega_4 = \omega_1 + \Delta_2 - \Delta_3$. Thus, expanding to the second order in $\Delta\omega$, we have that:

$$\begin{aligned} n_3 n_4 - n_1 n_2 &\simeq (\Delta_3 - \Delta_2) \Delta_3 \left[n_1 \partial_{\omega_1 \omega_1} n_1 - (\partial_{\omega_1} n_1)^2 \right] \\ &= (\Delta_3 - \Delta_2) \Delta_3 n_1^2 \frac{\partial^2}{\partial \omega_1^2} (\log n_1) \end{aligned} \quad (\text{D.4})$$

and

$$g(\omega_1) + g(\omega_2) - g(\omega_3) - g(\omega_4) \simeq (\Delta_2 - \Delta_3) \Delta_2 g''(\omega_1). \quad (\text{D.5})$$

By plugging these two results in (D.1) and integrating twice by parts, we obtain

$$\begin{aligned} &\int g(\omega) \left\{ \frac{\partial N}{\partial t} + \frac{\partial^2}{\partial \omega^2} \left[n^2 \frac{\partial^2}{\partial \omega^2} (\log n) \right] \right. \\ &\quad \left. \times \frac{1}{4} \int S_{\omega, \omega+\Delta_2}^{\omega+\Delta_3, \omega+\Delta_2-\Delta_3} \Delta_3^2 (\Delta_2 - \Delta_3)^2 d\Delta_{23} \right\} d\omega = 0 \end{aligned} \quad (\text{D.6})$$

where for simplicity we used ω instead of ω_1 . We now write $\Delta_i = \delta_i \omega$ with δ_i is a small number and obtain:

$$\int g(\omega) \left\{ \frac{\partial N}{\partial t} + \frac{\partial^2}{\partial \omega^2} \left[S \omega^{6+\chi} n^2 \frac{\partial^2}{\partial \omega^2} (\log n) \right] \right\} d\omega = 0, \quad (\text{D.7})$$

where χ is the degree of homogeneity of S_{12}^{34} and S is defined as:

$$S = \frac{1}{4} \int S_{1,1+\delta_2}^{1+\delta_3, 1+\delta_2-\delta_3} \delta_3^2 (\delta_2 - \delta_3)^2 d\delta_{23}. \quad (\text{D.8})$$

As (D.7) must be valid for every function g , this means that the DAM for the homogeneous isotropic Boltzmann equation in the three-dimensional hard sphere model is

$$\partial_t N(\omega, t) + \partial_{\omega\omega} R[n(\omega, t)] = 0, \quad (\text{D.9})$$

where

$$R[n(\omega, t)] = -S \omega^{\frac{13}{2}} n^2(\omega, t) \partial_{\omega\omega} \log n(\omega, t). \quad (\text{D.10})$$

Appendix E. Matching the Kats-Kontorovich to ω_{\max} front solution

We will here find the matching between the KK correction and the front solution for the ODE- ϵ . We make the hypothesis that the front occurs for $\omega_{\max} \gg T$ and so it is reasonable to think that the term $\omega^{-\frac{13}{2}}$ in Eq. (19) is slowly varying with respect to $e^{\frac{2\omega}{T}}$. So by integrating twice in ω (19) and match to the front we get the Cauchy problem:

$$\begin{cases} \epsilon \omega^{-\frac{13}{2}} \frac{T^2}{4} A^{-2} e^{\frac{2\omega}{T}} = -S \tilde{n} + c_1 (\omega - \omega_{\max}) + c_2 \\ \tilde{n}(\omega_{\max}) = -1 \\ \partial_{\omega} \tilde{n}(\omega_{\max}) = B A e^{\frac{\omega_{\max}}{T}}, \end{cases} \quad (\text{E.1})$$

where the first condition assures that $n(\omega_{\max}) = 0$ and the second that the front behavior is linear with the slope $B = -\epsilon^{\frac{1}{2}} \omega_{\max}^{-\frac{13}{4}}$ found in Eq. (17). The integration constants are then

$$\begin{cases} c_2 = -S + \epsilon \omega_{\max}^{-\frac{13}{2}} \frac{T^2}{4} A^{-2} e^{\frac{2\omega_{\max}}{T}} \\ c_1 = S^{-\frac{1}{2}} \epsilon^{\frac{1}{2}} \omega_{\max}^{-\frac{13}{4}} A^{-1} e^{\frac{\omega_{\max}}{T}} - \epsilon \omega_{\max}^{-\frac{13}{2}} \frac{T}{2} A^{-2} e^{\frac{2\omega_{\max}}{T}}. \end{cases} \quad (\text{E.2})$$

We will now match this solution in the regime where $T \ll \omega_{\max}$ and the flux is negligible with respect to the thermodynamic

solution. In this regime, by assuming the scaling relation $\epsilon \sim \omega_{\max}^{\frac{9}{2}} A^2 e^{-\frac{2\omega_{\max}}{T}}$, the coefficients results in

$$\begin{cases} c_2 \simeq -S \\ c_1 \simeq S^{-\frac{1}{2}} \epsilon^{\frac{1}{2}} \omega_{\max}^{-\frac{13}{4}} A^{-1} e^{\frac{\omega_{\max}}{T}} \end{cases} \quad (\text{E.3})$$

and so the smallness of the correction reads as

$$\begin{aligned} \tilde{n}(\omega) = 0 = & -\epsilon \omega^{-\frac{13}{2}} \frac{T^2}{4} A^{-2} e^{\frac{2\omega}{T}} \\ & + (\omega - \omega_{\max}) S^{-\frac{1}{2}} \epsilon^{\frac{1}{2}} \omega_{\max}^{-\frac{13}{4}} A^{-1} e^{\frac{\omega_{\max}}{T}} - S. \end{aligned} \quad (\text{E.4})$$

Finally, considering that $\omega \ll \omega_{\max}$, we recover and validate the relation

$$\epsilon = S \omega_{\max}^{\frac{9}{2}} A^2 e^{-\frac{2\omega_{\max}}{T}}. \quad (\text{E.5})$$

Appendix F. Matching the Kats–Kontorovich to ω_{\min} front solution

The KK correction for that case is given by Eq. (27). We will consider the limit $\omega \ll T$ and so $e^{\frac{2\omega}{T}} \simeq 1$. By integrating twice in ω we get the Cauchy problem

$$\begin{cases} |\eta| \omega^{-\frac{7}{2}} \frac{4}{63} A^{-2} = -S \tilde{n} + c_1 (\omega - \omega_{\min}) + c_2 \\ \tilde{n}(\omega_{\min}) = -1 \\ \partial_{\omega} \tilde{n}(\omega_{\min}) = |\eta|^{\frac{1}{2}} S \omega_{\min}^{-\frac{11}{4}} A^{-1} \end{cases} \quad (\text{F.1})$$

with the initial conditions chosen in order to match with the front solution. The integration constants result in

$$\begin{cases} c_2 = -S + |\eta| \omega_{\min}^{-\frac{7}{2}} \frac{4}{63} A^{-2} \\ c_1 = -S^{\frac{1}{2}} |\eta|^{\frac{1}{2}} \omega_{\min}^{-\frac{11}{4}} A^{-1} + |\eta| \omega_{\min}^{-\frac{9}{2}} \frac{2}{9} A^{-2}. \end{cases} \quad (\text{F.2})$$

We assume and guess that the particles flux scales as $|\eta| \sim \omega_{\min}^{\frac{7}{2}} A^2$. Now, in the regime $\omega \gg \omega_{\min}$ where the correction is negligible we have

$$\tilde{n}(\omega) = 0 = -|\eta| \omega^{-\frac{7}{2}} \frac{4}{63} A^{-2} + c_1 (\omega - \omega_{\min}) + c_2 \simeq \omega c_1. \quad (\text{F.3})$$

Finally, we impose that $c_1 = 0$ to get the condition on the flux

$$|\eta| = S \left(\frac{9}{2} \right)^2 A^2 \omega_{\min}^{\frac{7}{2}}. \quad (\text{F.4})$$

Appendix G. Scaling properties of the DAM

The constant energy flux DAM (15) and the constant particles flux DAM (24) can be generally written as

$$c = -S \omega^p n^2(\omega) \partial_{\omega} \log n(\omega) \quad (\text{G.1})$$

where the exponent is respectively $p = 13/2$ and $p = 11/2$ and c is a constant that represent the considered flux. Let us now analyze the rescaling properties of that equation by the following change of variables

$$\begin{cases} c = \lambda^{\alpha} \bar{c} \\ \omega = \lambda^{\beta} \bar{\omega} \\ n = \lambda^{\gamma} \bar{n}. \end{cases} \quad (\text{G.2})$$

After some easy algebra we find that the system is invariant if

$$\alpha = (p - 2)\beta + 2\gamma. \quad (\text{G.3})$$

As a consequence we can establish how the thermodynamic quantities defined by the Maxwell–Boltzmann distribution $n_{\text{MB}}(\omega) = A e^{-\frac{\omega}{T}} = e^{-\frac{\omega+T}{T}}$ vary: the temperature T scales as ω and so $T = \lambda^{\beta} \bar{T}$, while the chemical potential μ scales as $\mu = \lambda^{\beta} \gamma \bar{\mu}$.

References

- [1] C. Bustamante, J. Liphardt, F. Ritort, The nonequilibrium thermodynamics of small systems, *Phys. Today* 58 (7) (2005) 43–48. doi:10.1063/1.2012462. URL: <http://link.aip.org/link/?PTO/58/43/1>.
- [2] E.H. Lieb, Some problems in statistical mechanics that I would like to see solved, *Physica A* 263 (1–4) (1999) 491–499. doi:10.1016/S0378-4371(98)00517-2. Proceedings of the 20th IUPAP International Conference on Statistical Physics. URL: <http://www.sciencedirect.com/science/article/B6TVG-3YGKSSR-1R/2/4deb7bfa0074a6a1930a8fc21deed508>.
- [3] T.S. Komatsu, N. Nakagawa, S.-i. Sasa, H. Tasaki, Steady-state thermodynamics for heat conduction: microscopic derivation, *Phys. Rev. Lett.* 100 (23) (2008) 230602. doi:10.1103/PhysRevLett.100.230602.
- [4] C. Cercignani, *The Boltzmann Equation and its Applications*, Springer, 1988.
- [5] V. Zakharov, V. L'vov, Falkovich, *Kolmogorov Spectra of Turbulence 1: Wave Turbulence*, Springer-Verlag, 1992.
- [6] A. Kolmogorov, The local structure of turbulence in an incompressible fluid for very large wave numbers, in: *Proceedings (Doklady) Academy of Sciences, USSR*, Vol. 30, 1941, pp. 301–305.
- [7] U. Frisch, *Turbulence: The Legacy of AN Kolmogorov*, Cambridge University Press, 1995.
- [8] P. Janssen, *The Interaction of Ocean Waves and Wind*, Cambridge University Press, 2004.
- [9] M. Onorato, A. Osborne, M. Serio, D. Resio, A. Pushkarev, V. Zakharov, C. Brandini, Freely decaying weak turbulence for sea surface gravity waves, *Phys. Rev. Lett.* 89 (14) (2002) 144501.
- [10] A. Dyachenko, A. Korotkevich, V. Zakharov, Weak turbulence of gravity waves, *J. Exp. Theor. Phys. Lett.* 77 (10) (2003) 546–550.
- [11] Y. Lvov, K. Polzin, E. Tabak, Energy spectra of the ocean's internal wave field: theory and observations, *Phys. Rev. Lett.* 92 (12) (2004) 128501.
- [12] S. Dyachenko, A.C. Newell, A. Pushkarev, V.E. Zakharov, Optical turbulence: weak turbulence, condensates and collapsing filaments in the nonlinear Schrödinger equation, *Physica D* 57 (1–2) (1992) 96–160. URL: <http://www.sciencedirect.com/science/article/B6TVK-46JH21H-4G/2/b9bf3a47086f6f154a8c0478ca64c07b>.
- [13] N. Berloff, B. Svistunov, Scenario of strongly nonequilibrated Bose–Einstein condensation, *Phys. Rev. A* 66 (1) (2002) 13603.
- [14] S. Nazarenko, M. Onorato, Wave turbulence and vortices in Bose–Einstein condensation, *Physica D* 219 (1) (2006) 1–12.
- [15] D. Proment, S. Nazarenko, M. Onorato, Quantum turbulence cascades in the Gross–Pitaevskii model, *Phys. Rev. A* 80 (5) (2009) 051603. doi:10.1103/PhysRevA.80.051603.
- [16] S. Galtier, S. Nazarenko, A. Newell, A. Pouquet, A weak turbulence theory for incompressible magnetohydrodynamics, *J. Plasma Phys.* 63 (05) (2000) 447–488.
- [17] A. Kats, V. Kontorovich, S. Moiseev, V. Novikov, Power-law solutions of the Boltzmann kinetic equation, describing the spectral distribution of particles with fluxes, *ZhETF Pis ma Redaktiiu* 21 (1) (1975) 13–16. (English version comes from JETP Lett. 21 (1) (1975) 5–6).
- [18] A. Kats, Direction of transfer of energy and quasi-particle number along the spectrum in stationary power-law solutions of the kinetic equations for waves and particles, *Sov. J. Exp. Theoret. Phys.* 44 (1976) 1106.
- [19] C. Connaughton, S. Nazarenko, Warm cascades and anomalous scaling in a diffusion model of turbulence, *Phys. Rev. Lett.* 92 (4) (2004) 044501. doi:10.1103/PhysRevLett.92.044501.
- [20] L. Pitaevskii, S. Stringari, *Bose–Einstein Condensation*, vol. 116, Oxford University Press, USA, 2003.
- [21] A. Griffin, T. Nikuni, E. Zaremba, *Bose-Condensed Gases at Finite Temperatures*, Cambridge University Press, 2009.
- [22] N. Brilliantov, T. Poschel, *Kinetic Theory of Granular Gases*, Oxford University Press, USA, 2004.
- [23] V. Karas, S. Moiseev, V. Novikov, Nonequilibrium stationary distribution of particles in a solid plasma, *Zh. Eksp. Teor. Fiz.* 71 (1976) 1421–1433.
- [24] C. Connaughton, S. Nazarenko, A.C. Newell, Dimensional analysis and weak turbulence, *Physica D* 184 (1–4) (2003) 86–97. URL: <http://www.sciencedirect.com/science/article/B6TVK-49CRR6J-1/2/278d7b4065f6440d2117abc08ee9ac48>.
- [25] A. Balk, On the Kolmogorov–Zakharov spectra of weak turbulence, *Physica D* 139 (1–2) (2000) 137–157.
- [26] N.P. Proukakis, B. Jackson, Finite-temperature models of Bose–Einstein condensation, *J. Phys. B* 41 (20) (2008) 203002. URL: <http://stacks.iop.org/0953-4075/41/i=20/a=203002>.
- [27] F. Rouyer, N. Menon, Velocity fluctuations in a homogeneous 2D granular gas in steady state, *Phys. Rev. Lett.* 85 (2000) 3676–3679. doi:10.1103/PhysRevLett.85.3676. URL: <http://link.aps.org/doi/10.1103/PhysRevLett.85.3676>.
- [28] E. Ben-Naim, J. Machta, Stationary states and energy cascades in inelastic gases, *Phys. Rev. Lett.* 94 (2005) 138001. doi:10.1103/PhysRevLett.94.138001. URL: <http://link.aps.org/doi/10.1103/PhysRevLett.94.138001>.
- [29] W. Kang, J. Machta, E. Ben-Naim, Granular gases under extreme driving, *Europhys. Lett.* EPL 91 (3) (2010) 34002. URL: <http://stacks.iop.org/0295-5075/91/i=3/a=34002>.

- [30] C. Connaughton, Numerical solutions of the isotropic 3-wave kinetic equation, *Physica D* 238 (23–24) (2009) 2282–2297. doi:10.1016/j.physd.2009.09.012. URL: <http://www.sciencedirect.com/science/article/B6TVK-4X85F57-1/2/e0db658e124585ac3a87437017414d85>.
- [31] S. Hasselmann, K. Hasselmann, J. Allender, T. Barnett, Computations and parameterizations of the nonlinear energy transfer in a gravity-wave spectrum. Part II: parameterizations of the nonlinear energy transfer for application in wave models, *J. Phys. Oceanogr.* 15 (11) (1985) 1378–1391.
- [32] C.E. Leith, Diffusion approximation to inertial energy transfer in isotropic turbulence, *Phys. Fluids* 10 (7) (1967) 1409–1416. doi:10.1063/1.1762300. URL: <http://link.aip.org/link/?PFL/10/1409/1>.
- [33] V. L'vov, S. Nazarenko, Differential model for 2D turbulence, *JETP Lett.* 83 (12) (2006) 541–545.
- [34] C. Connaughton, R. McAdams, Mixed flux-equipartition solutions of a diffusion model of nonlinear cascades, *Europhys. Lett.* EPL 95 (2) (2011) 24005. URL: <http://stacks.iop.org/0295-5075/95/i=2/a=24005>.
- [35] G. Boffetta, A. Celani, D. Dezzani, J. Laurie, S. Nazarenko, Modeling kelvin wave cascades in superfluid helium, *J. Low Temp. Phys.* 156 (3) (2009) 193–214.
- [36] J. Peacock, *Cosmological Physics*, Cambridge Univ. Pr., 1999.
- [37] Y. Lvov, R. Binder, A. Newell, Quantum weak turbulence with applications to semiconductor lasers, *Physica D* 121 (3–4) (1998) 317–343.
- [38] V. Zakharov, A. Pushkarev, Diffusion model of interacting gravity waves on the surface of deep fluid, *Nonlinear Processes Geophys.* 6 (1999) 1–10.
- [39] D. Proment, S. Nazarenko, P. Asinari, M. Onorato, Warm turbulence in the Boltzmann equation, *Europhys. Lett.* 96 (2) (2011) 24004.
- [40] P. Asinari, Nonlinear Boltzmann equation for the homogeneous isotropic case: minimal deterministic matlab program, *Comput. Phys. Comm.* 181 (10) (2010) 1776–1788. doi:10.1016/j.cpc.2010.06.041. URL: <http://www.sciencedirect.com/science/article/B6TJ5-50HP2XY-4/2/31b9575c0bbef1cba9ce59798563cc5f>.
- [41] A.C. Newell, S. Nazarenko, L. Biven, Wave turbulence and intermittency, *Physica D* 152–153 (2001) 520–550. doi:10.1016/S0167-2789(01)00192-0. URL: <http://www.sciencedirect.com/science/article/B6TVK-430G97Y-1V/2/7539b751b3e972419ca247108cd8d56c>.
- [42] S. Harris, *An Introduction to the Theory of the Boltzmann Equation*, Dover Publications, 2004.